

Searching for stochastic gravitational waves using data from the two colocated LIGO Hanford detectors

J. Aasi,¹ J. Abadie,¹ B. P. Abbott,¹ R. Abbott,¹ T. Abbott,² M. R. Abernathy,¹ T. Accadia,³ F. Acernese,^{4,5} C. Adams,⁶ T. Adams,⁷ P. Addesso,⁸ R. X. Adhikari,¹ C. Affeldt,⁹ M. Agathos,¹⁰ N. Aggarwal,¹¹ O. D. Aguiar,¹² P. Ajith,¹ B. Allen,^{9,13,14} A. Allocca,^{15,16} E. Amador Ceron,¹³ D. Amariutei,¹⁷ R. A. Anderson,¹ S. B. Anderson,¹ W. G. Anderson,¹³ K. Arai,¹ M. C. Araya,¹ C. Arceneaux,¹⁸ J. Areeda,¹⁹ S. Ast,¹⁴ S. M. Aston,⁶ P. Astone,²⁰ P. Aufmuth,¹⁴ C. Aulbert,⁹ L. Austin,¹ B. E. Aylott,²¹ S. Babak,²² P. T. Baker,²³ G. Ballardín,²⁴ S. W. Ballmer,²⁵ J. C. Barayoga,¹ D. Barker,²⁶ S. H. Barnum,¹¹ F. Barone,^{4,5} B. Barr,²⁷ L. Barsotti,¹¹ M. Barsuglia,²⁸ M. A. Barton,²⁶ I. Bartos,²⁹ R. Bassiri,^{30,27} A. Basti,^{31,16} J. Batch,²⁶ J. Bauchrowitz,⁹ Th. S. Bauer,¹⁰ M. Bebronne,³ B. Behnke,²² M. Bejger,³² M. G. Beker,¹⁰ A. S. Bell,²⁷ C. Bell,²⁷ I. Belopolski,²⁹ G. Bergmann,⁹ J. M. Berliner,²⁶ D. Bersanetti,^{33,34} A. Bertolini,¹⁰ D. Bessis,³⁵ J. Betzwieser,⁶ P. T. Beyersdorf,³⁶ T. Bhadhbhade,³⁰ I. A. Bilenko,³⁷ G. Billingsley,¹ J. Birch,⁶ S. Biscans,¹¹ M. Bitossi,¹⁶ M. A. Bizouard,³⁸ E. Black,¹ J. K. Blackburn,¹ L. Blackburn,³⁹ D. Blair,⁴⁰ M. Blom,¹⁰ O. Bock,¹⁰ T. P. Bodiya,¹¹ M. Boer,⁴¹ C. Bogan,⁹ C. Bond,²¹ F. Bondu,⁴² L. Bonelli,^{31,16} R. Bonnand,⁴³ R. Bork,¹ M. Born,⁹ V. Boschi,¹⁶ S. Bose,⁴⁴ L. Bosi,⁴⁵ J. Bowers,² C. Bradaschia,¹⁶ P. R. Brady,¹³ V. B. Braginsky,³⁷ M. Branchesi,^{46,47} C. A. Brannen,⁴⁴ J. E. Brau,⁴⁸ J. Breyer,⁹ T. Briant,⁴⁹ D. O. Bridges,⁶ A. Brillet,⁴¹ M. Brinkmann,⁹ V. Brisson,³⁸ M. Britzger,⁹ A. F. Brooks,¹ D. A. Brown,²⁵ D. D. Brown,²¹ F. Brückner,²¹ T. Bulik,⁵⁰ H. J. Bulten,^{51,10} A. Buonanno,⁵² D. Buskulic,³ C. Buy,²⁸ R. L. Byer,³⁰ L. Cadonati,⁵³ G. Cagnoli,⁴³ J. Calderón Bustillo,⁵⁴ E. Calloni,^{55,5} J. B. Camp,³⁹ P. Campsie,²⁷ K. C. Cannon,⁵⁶ B. Canuel,²⁴ J. Cao,⁵⁷ C. D. Capano,⁵² F. Carbognani,²⁴ L. Carbone,²¹ S. Caride,⁵⁸ A. Castiglia,⁵⁹ S. Caudill,¹³ M. Cavaglia,¹⁸ F. Cavalier,³⁸ R. Cavalieri,²⁴ G. Cella,¹⁶ C. Cepeda,¹ E. Cesarini,⁶⁰ R. Chakraborty,¹ T. Chalmersongsak,¹ S. Chao,⁶¹ P. Charlton,⁶² E. Chassande-Mottin,²⁸ X. Chen,⁴⁰ Y. Chen,⁶³ A. Chincarini,³⁴ A. Chiummo,²⁴ H. S. Cho,⁶⁴ J. Chow,⁶⁵ N. Christensen,⁶⁶ Q. Chu,⁴⁰ S. S. Y. Chua,⁶⁵ S. Chung,⁴⁰ G. Ciani,¹⁷ F. Clara,²⁶ D. E. Clark,³⁰ J. A. Clark,⁵³ F. Cleva,⁴¹ E. Coccia,^{67,60} P.-F. Cohadon,⁴⁹ A. Colla,^{68,20} M. Colombini,⁴⁵ M. Constanancio, Jr.,¹² A. Conte,^{68,20} D. Cook,²⁶ T. R. Corbitt,² M. Cordier,³⁶ N. Cornish,²³ A. Corsi,⁶⁹ C. A. Costa,¹² M. W. Coughlin,⁷⁰ J.-P. Coulon,⁴¹ S. Countryman,²⁹ P. Couvares,²⁵ D. M. Coward,⁴⁰ M. Cowart,⁶ D. C. Coyne,¹ K. Craig,²⁷ J. D. E. Creighton,¹³ T. D. Creighton,³⁵ S. G. Crowder,⁷¹ A. Cumming,²⁷ L. Cunningham,²⁷ E. Cuoco,²⁴ K. Dahl,⁹ T. Dal Canton,⁹ M. Damjanic,⁹ S. L. Danilishin,⁴⁰ S. D'Antonio,⁶⁰ K. Danzmann,^{9,14} V. Dattilo,²⁴ B. Daudert,¹ H. Daveloza,³⁵ M. Davies,³⁸ G. S. Davies,²⁷ E. J. Daw,⁷² R. Day,²⁴ T. Dayanga,⁴⁴ G. Debreczeni,⁷³ J. Degallaix,⁴³ E. Deleueu,¹⁷ S. Deléglise,⁴⁹ W. Del Pozzo,¹⁰ T. Denker,⁹ T. Dent,⁹ H. Dereli,⁴¹ V. Dergachev,¹ R. T. DeRosa,² R. De Rosa,^{55,5} R. DeSalvo,⁷⁴ S. Dhurandhar,⁷⁵ M. Díaz,³⁵ A. Dietz,¹⁸ L. Di Fiore,⁵ A. Di Lieto,^{31,16} I. Di Palma,⁹ A. Di Virgilio,¹⁶ K. Dmitry,³⁷ F. Donovan,¹¹ K. L. Dooley,⁹ S. Doravari,⁶ M. Drago,^{76,77} R. W. P. Drever,⁷⁸ J. C. Driggers,¹ Z. Du,⁵⁷ J.-C. Dumas,⁴⁰ S. Dwyer,²⁶ T. Eberle,⁹ M. Edwards,⁷ A. Effler,² P. Ehrens,¹ J. Eichholz,¹⁷ S. S. Eikenberry,¹⁷ G. Endrőczy,⁷³ R. Essick,¹¹ T. Etzel,¹ K. Evans,²⁷ M. Evans,¹¹ T. Evans,⁶ M. Factourovich,²⁹ V. Fafone,^{67,60} S. Fairhurst,⁷ Q. Fang,⁴⁰ B. Farr,⁷⁹ W. Farr,⁷⁹ M. Favata,⁸⁰ D. Fazi,⁷⁹ H. Fehrmann,⁹ D. Feldbaum,^{17,6} I. Ferrante,^{31,16} F. Ferrini,²⁴ F. Fidecaro,^{31,16} L. S. Finn,⁸¹ I. Fiori,²⁴ R. Fisher,²⁵ R. Flaminio,⁴³ E. Foley,¹⁹ S. Foley,¹¹ E. Forsi,⁶ N. Fotopoulos,¹ J.-D. Fournier,⁴¹ S. Franco,³⁸ S. Frasca,^{68,20} F. Frasconi,¹⁶ M. Frede,⁹ M. Frei,⁵⁹ Z. Frei,⁸² A. Freise,²¹ R. Frey,⁴⁸ T. T. Fricke,⁹ P. Fritschel,¹¹ V. V. Frolov,⁶ M.-K. Fujimoto,⁸³ P. Fulda,¹⁷ M. Fyffe,⁶ J. Gair,⁷⁰ L. Gammaitoni,^{84,45} J. Garcia,²⁶ F. Garufi,^{55,5} N. Gehrels,³⁹ G. Gemme,³⁴ E. Genin,²⁴ A. Gennai,¹⁶ L. Gergely,⁸⁵ S. Ghosh,⁴⁴ J. A. Giaime,^{2,6} S. Giampanis,¹³ K. D. Giardino,⁶ A. Giazotto,¹⁶ S. Gil-Casanova,⁵⁴ C. Gill,²⁷ J. Gleason,¹⁷ E. Goetz,⁹ R. Goetz,¹⁷ L. Gondan,⁸² G. González,² N. Gordon,²⁷ M. L. Gorodetsky,³⁷ S. Gossan,⁶³ S. Goßler,⁹ R. Gouaty,³ C. Graef,⁹ P. B. Graff,³⁹ M. Granata,⁴³ A. Grant,²⁷ S. Gras,¹¹ C. Gray,²⁶ R. J. S. Greenhalgh,⁸⁶ A. M. Gretarsson,⁸⁷ C. Griffo,¹⁹ H. Grote,⁹ K. Grover,²¹ S. Grunewald,²² G. M. Guidi,^{46,47} C. Guido,⁶ K. E. Gushwa,¹ E. K. Gustafson,¹ R. Gustafson,⁵⁸ B. Hall,⁴⁴ E. Hall,¹ D. Hammer,¹³ G. Hammond,²⁷ M. Hanke,⁹ J. Hanks,²⁶ C. Hanna,⁸⁸ J. Hanson,⁶ J. Harms,¹ G. M. Harry,⁸⁹ I. W. Harry,²⁵ E. D. Harstad,⁴⁸ M. T. Hartman,¹⁷ K. Haughian,²⁷ K. Hayama,⁸³ J. Heefner,¹ A. Heidmann,⁴⁹ M. Heintze,^{17,6} H. Heitmann,⁴¹ P. Hello,³⁸ G. Hemming,²⁴ M. Hendry,²⁷ I. S. Heng,²⁷ A. W. Heptonstall,¹ M. Heurs,⁹ S. Hild,²⁷ D. Hoak,⁵³ K. A. Hodge,¹ K. Holt,⁶ T. Hong,⁶³ S. Hooper,⁴⁰ T. Horrom,⁹⁰ D. J. Hosken,⁹¹ J. Hough,²⁷ E. J. Howell,⁴⁰ Y. Hu,²⁷ Z. Hua,⁵⁷ V. Huang,⁶¹ E. A. Huerta,²⁵ B. Hughey,⁸⁷ S. Husa,⁵⁴ S. H. Huttner,²⁷ M. Huynh,¹³ T. Huynh-Dinh,⁶ J. Iafrate,² D. R. Ingram,²⁶ R. Inta,⁶⁵ T. Isogai,¹¹ A. Ivanov,¹ B. R. Iyer,⁹² K. Izumi,²⁶ M. Jacobson,¹ E. James,¹ H. Jang,⁹³ Y. J. Jang,⁷⁹ P. Jananowski,⁹⁴ F. Jiménez-Forteza,⁵⁴ W. W. Johnson,² D. I. Jones,⁹⁵ D. Jones,²⁶ R. Jones,²⁷ R. J. G. Jonker,¹⁰ L. Ju,⁴⁰ Haris K.,⁹⁶ P. Kalmus,¹ V. Kalogera,⁷⁹ S. Kandhasamy,^{18,71,*} G. Kang,⁹³ J. B. Kanner,³⁹ M. Kasprzack,^{38,24} R. Kasturi,⁹⁷ E. Katsavounidis,¹¹ W. Katzman,⁶ H. Kaufer,¹⁴ K. Kaufman,⁶³ K. Kawabe,²⁶ S. Kawamura,⁸³ F. Kawazoe,⁹ F. Kéfélian,⁴¹ D. Keitel,⁹ D. B. Kelley,²⁵ W. Kells,¹ D. G. Keppel,⁹ A. Khalaidovski,⁹ F. Y. Khalili,³⁷ E. A. Khazanov,⁹⁸ B. K. Kim,⁹³ C. Kim,^{99,93} K. Kim,¹⁰⁰ N. Kim,³⁰ W. Kim,⁹¹ Y.-M. Kim,⁶⁴ E. King,⁹¹ P. J. King,¹ D. L. Kinzel,⁶ J. S. Kissel,¹¹ S. Klimenko,¹⁷ J. Kline,¹³ S. Koehlenbeck,⁹ K. Kokeyama,² V. Kondrashov,¹ S. Koranda,¹³ W. Z. Korth,¹ I. Kowalska,⁵⁰ D. Kozak,¹ A. Kremin,⁷¹ V. Kringel,⁹ B. Krishnan,⁹ A. Królak,^{101,102} C. Kucharczyk,³⁰ S. Kudla,² G. Kuehn,⁹ A. Kumar,¹⁰³ D. Nanda Kumar,¹⁷ P. Kumar,²⁵ R. Kumar,²⁷ R. Kurdyumov,³⁰ P. Kwee,¹¹ M. Landry,²⁶ B. Lantz,³⁰ S. Larson,¹⁰⁴

P. D. Lasky,¹⁰⁵ C. Lawrie,²⁷ A. Lazzarini,¹ P. Leaci,²² E. O. Lebigot,⁵⁷ C.-H. Lee,⁶⁴ H. K. Lee,¹⁰⁰ H. M. Lee,⁹⁹ J. J. Lee,¹⁹ J. Lee,¹¹ M. Leonardi,^{76,77} J. R. Leong,⁹ A. Le Roux,⁶ N. Leroy,³⁸ N. Letendre,³ B. Levine,²⁶ J. B. Lewis,¹ V. Lhuillier,²⁶ T. G. F. Li,¹⁰ A. C. Lin,³⁰ T. B. Littenberg,⁷⁹ V. Litvine,¹ F. Liu,¹⁰⁶ H. Liu,⁷ Y. Liu,⁵⁷ Z. Liu,¹⁷ D. Lloyd,¹ N. A. Lockerbie,¹⁰⁷ V. Lockett,¹⁹ D. Lodhia,²¹ K. Loew,⁸⁷ J. Logue,²⁷ A. L. Lombardi,⁵³ M. Lorenzini,^{67,60} V. Lorient,¹⁰⁸ M. Lormand,⁶ G. Losurdo,⁴⁷ J. Lough,²⁵ J. Luan,⁶³ M. J. Lubinski,²⁶ H. Lück,^{9,14} A. P. Lundgren,⁹ J. Macarthur,²⁷ E. Macdonald,⁷ B. Machenschalk,⁹ M. MacInnis,¹¹ D. M. Macleod,⁷ F. Magana-Sandoval,¹⁹ M. Mageswaran,¹ K. Mailand,¹ E. Majorana,²⁰ I. Maksimovic,¹⁰⁸ V. Malvezzi,^{67,60} N. Man,⁴¹ G. M. Manca,⁹ I. Mandel,²¹ V. Mandic,⁷¹ V. Mangano,^{68,20} M. Mantovani,¹⁶ F. Marchesoni,^{109,45} F. Marion,³ S. Márka,²⁹ Z. Márka,²⁹ A. Markosyan,³⁰ E. Maros,¹ J. Marque,²⁴ F. Martelli,^{46,47} L. Martellini,⁴¹ I. W. Martin,²⁷ R. M. Martin,¹⁷ G. Martini,¹ D. Martynov,¹ J. N. Marx,¹ K. Mason,¹¹ A. Masserot,³ T. J. Massinger,²⁵ F. Matichard,¹¹ L. Matone,²⁹ R. A. Matzner,¹¹⁰ N. Mavalvala,¹¹ G. May,² N. Mazumder,⁹⁶ G. Mazzolo,⁹ R. McCarthy,²⁶ D. E. McClelland,⁶⁵ S. C. McGuire,¹¹¹ G. McIntyre,¹ J. McIver,⁵³ D. Meacher,⁴¹ G. D. Meadors,⁵⁸ M. Mehmet,⁹ J. Meidam,¹⁰ T. Meier,¹⁴ A. Melatos,¹⁰⁵ G. Mendell,²⁶ R. A. Mercer,¹³ S. Meshkov,¹ C. Messenger,²⁷ M. S. Meyer,⁶ H. Miao,⁶³ C. Michel,⁴³ E. Mikhailov,⁹⁰ L. Milano,^{55,5} J. Miller,⁶⁵ Y. Minenkov,⁶⁰ C. M. F. Mingarelli,²¹ S. Mitra,⁷⁵ V. P. Mitrofanov,³⁷ G. Mitselmakher,¹⁷ R. Mittleman,¹¹ B. Moe,¹³ M. Mohan,²⁴ S. R. P. Mohapatra,^{25,59} F. Mokler,⁹ D. Moraru,²⁶ G. Moreno,²⁶ N. Morgado,⁴³ T. Mori,⁸³ S. R. Morriss,³⁵ K. Mossavi,⁹ B. Mours,³ C. M. Mow-Lowry,⁹ C. L. Mueller,¹⁷ G. Mueller,¹⁷ S. Mukherjee,³⁵ A. Mullavey,² J. Munch,⁹¹ D. Murphy,²⁹ P. G. Murray,²⁷ A. Mytidis,¹⁷ M. F. Nagy,⁷³ I. Nardecchia,^{67,60} T. Nash,¹ L. Naticchioni,^{68,20} R. Nayak,¹¹² V. Necula,¹⁷ I. Neri,^{84,45} M. Neri,^{33,34} G. Newton,²⁷ T. Nguyen,⁶⁵ E. Nishida,⁸³ A. Nishizawa,⁸³ A. Nitz,²⁵ F. Nocera,²⁴ D. Nolting,⁶ M. E. Normandin,³⁵ L. K. Nuttall,⁷ E. Ochsner,¹³ J. O'Dell,⁸⁶ E. Oelker,¹¹ G. H. Ogin,¹ J. J. Oh,¹¹³ S. H. Oh,¹¹³ F. Ohme,⁷ P. Oppermann,⁹ B. O'Reilly,⁶ W. Ortega Larcher,³⁵ R. O'Shaughnessy,¹³ C. Osthelder,¹ D. J. Ottaway,⁹¹ R. S. Ottens,¹⁷ J. Ou,⁶¹ H. Overmier,⁶ B. J. Owen,⁸¹ C. Padilla,¹⁹ A. Pai,⁹⁶ C. Palomba,²⁰ Y. Pan,⁵² C. Pankow,¹³ F. Paoletti,^{24,16} R. Paoletti,^{15,16} H. Paris,²⁶ A. Pasqualetti,²⁴ R. Passaquieti,^{31,16} D. Passuello,¹⁶ M. Pedraza,¹ P. Peiris,⁵⁹ S. Penn,⁹⁷ A. Perreca,²⁵ M. Phelps,¹ M. Pichot,⁴¹ M. Pickenpack,⁹ F. Piergiovanni,^{46,47} V. Pierro,⁷⁴ L. Pinard,⁴³ B. Pindor,¹⁰⁵ I. M. Pinto,⁷⁴ M. Pitkin,²⁷ J. Poeld,⁹ R. Poggiani,^{31,16} V. Poole,⁴⁴ F. Postiglione,⁸ C. Poux,¹ V. Predoi,⁷ T. Prestegard,⁷¹ L. R. Price,¹ M. Prijatelj,⁹ S. Privitera,¹ G. A. Prodi,^{76,77} L. Prokhorov,³⁷ O. Puncken,³⁵ M. Punturo,⁴⁵ P. Puppò,²⁰ V. Quetschke,³⁵ E. Quintero,¹ R. Quitzow-James,⁴⁸ F. J. Raab,²⁶ D. S. Rabeling,^{51,10} I. Rácz,⁷³ H. Radkins,²⁶ P. Raffai,^{29,82} S. Raja,¹¹⁴ G. Rajalakshmi,¹¹⁵ M. Rakhmanov,³⁵ C. Ramet,⁶ P. Rapagnani,^{68,20} V. Raymond,¹ V. Re,^{67,60} C. M. Reed,²⁶ T. Reed,¹¹⁶ T. Regimbau,⁴¹ S. Reid,¹¹⁷ D. H. Reitze,^{1,17} F. Ricci,^{68,20} R. Riesen,⁶ K. Riles,⁵⁸ N. A. Robertson,^{1,27} F. Robinet,³⁸ A. Rocchi,⁶⁰ S. Roddy,⁶ C. Rodriguez,⁷⁹ M. Rodruck,²⁶ C. Roever,⁹ L. Rolland,³ J. G. Rollins,¹ J. D. Romano,³⁵ R. Romano,^{4,5} G. Romanov,⁹⁰ J. H. Romie,⁶ D. Rosińska,^{118,32} S. Rowan,²⁷ A. Rüdiger,⁹ P. Ruggi,²⁴ K. Ryan,²⁶ F. Salemi,⁹ L. Sammut,¹⁰⁵ V. Sandberg,²⁶ J. Sanders,⁵⁸ V. Sannibale,¹ I. Santiago-Prieto,²⁷ E. Saracco,⁴³ B. Sassolas,⁴³ B. S. Sathyaprakash,⁷ P. R. Saulson,²⁵ R. Savage,²⁶ R. Schilling,⁹ R. Schnabel,^{9,14} R. M. S. Schofield,⁴⁸ E. Schreiber,⁹ D. Schuette,⁹ B. Schulz,⁹ B. F. Schutz,^{22,7} P. Schwinberg,²⁶ J. Scott,²⁷ S. M. Scott,⁶⁵ F. Seifert,¹ D. Sellers,⁶ A. S. Sengupta,¹¹⁹ D. Sentenac,²⁴ V. Sequino,^{67,60} A. Sergeev,⁹⁸ D. Shaddock,⁶⁵ S. Shah,^{10,120} M. S. Shahrar,⁷⁹ M. Shaltev,⁹ B. Shapiro,³⁰ P. Shawhan,⁵² D. H. Shoemaker,¹¹ T. L. Sidery,²¹ K. Siellez,⁴¹ X. Siemens,¹³ D. Sigg,²⁶ D. Simakov,⁹ A. Singer,¹ L. Singer,¹ A. M. Sintes,⁵⁴ G. R. Skelton,¹³ B. J. J. Slagmolen,⁶⁵ J. Slutsky,⁹ J. R. Smith,¹⁹ M. R. Smith,¹ R. J. E. Smith,²¹ N. D. Smith-Lefebvre,¹ K. Soden,¹³ E. J. Son,¹¹³ B. Sorazu,²⁷ T. Souradeep,⁷⁵ L. Sperandio,^{67,60} A. Staley,²⁹ E. Steinert,²⁶ J. Steinlechner,⁹ S. Steinlechner,⁹ S. Steplewski,⁴⁴ D. Stevens,⁷⁹ A. Stochino,⁶⁵ R. Stone,³⁵ K. A. Strain,²⁷ N. Straniero,⁴³ S. Strigin,³⁷ A. S. Stroer,³⁵ R. Sturani,^{46,47} A. L. Stuver,⁶ T. Z. Summerscales,¹²¹ S. Susmithan,⁴⁰ P. J. Sutton,⁷ B. Swinkels,²⁴ G. Szeifert,⁸² M. Tacca,²⁸ D. Talukder,⁴⁸ L. Tang,³⁵ D. B. Tanner,¹⁷ S. P. Tarabrin,⁹ R. Taylor,¹ A. P. M. ter Braack,¹⁰ M. P. Thirugnanasambandam,¹ M. Thomas,⁶ P. Thomas,²⁶ K. A. Thorne,⁶ K. S. Thorne,⁶³ E. Thrane,¹ V. Tiwari,¹⁷ K. V. Tokmakov,¹⁰⁷ C. Tomlinson,⁷² A. Toncelli,^{31,16} M. Tonelli,^{31,16} O. Torre,^{15,16} C. V. Torres,³⁵ C. I. Torrie,^{1,27} F. Travasso,^{84,45} G. Traylor,⁶ M. Tse,²⁹ D. Ugolini,¹²² C. S. Unnikrishnan,¹¹⁵ H. Vahlbruch,¹⁴ G. Vajente,^{31,16} M. Vallisneri,⁶³ J. F. J. van den Brand,^{51,10} C. Van Den Broeck,¹⁰ S. van der Putten,¹⁰ M. V. van der Sluys,⁷⁹ J. van Heijningen,¹⁰ A. A. van Veggel,²⁷ S. Vass,¹ M. Vasúth,⁷³ R. Vaulin,¹¹ A. Vecchio,²¹ G. Vedovato,¹²³ P. J. Veitch,⁹¹ J. Veitch,¹⁰ K. Venkateswara,¹²⁴ D. Verkindt,³ S. Verma,⁴⁰ F. Vetrano,^{46,47} A. Viceré,^{46,47} R. Vincent-Finley,¹¹¹ J.-Y. Vinet,⁴¹ S. Vitale,¹¹ S. Vitale,¹⁰ B. Vlcek,¹³ T. Vo,²⁶ H. Vocca,^{84,45} C. Vorvick,²⁶ W. D. Vousden,²¹ D. Vrinceanu,³⁵ S. P. Vyachanin,³⁷ A. Wade,⁶⁵ L. Wade,¹³ M. Wade,¹³ S. J. Waldman,¹¹ M. Walker,² L. Wallace,¹ Y. Wan,⁵⁷ J. Wang,⁶¹ M. Wang,²¹ X. Wang,⁵⁷ A. Wanner,⁹ R. L. Ward,⁶⁵ M. Was,⁹ B. Weaver,²⁶ L.-W. Wei,⁴¹ M. Weinert,⁹ A. J. Weinstein,¹ R. Weiss,¹¹ T. Welborn,⁶ L. Wen,⁴⁰ P. Wessels,⁹ M. West,²⁵ T. Westphal,⁹ K. Wette,⁹ J. T. Whelan,⁵⁹ D. J. White,⁷² B. F. Whiting,¹⁷ S. Wibowo,¹³ K. Wiesner,⁹ C. Wilkinson,²⁶ L. Williams,¹⁷ R. Williams,¹ T. Williams,¹²⁵ J. L. Willis,¹²⁶ B. Willke,^{9,14} M. Wimmer,⁹ L. Winkelmann,⁹ W. Winkler,⁹ C. C. Wipf,¹¹ H. Wittel,⁹ G. Woan,²⁷ J. Worden,²⁶ J. Yablon,⁷⁹ I. Yakushin,⁶ H. Yamamoto,¹ C. C. Yancey,⁵² H. Yang,⁶³ D. Yeaton-Massey,¹ S. Yoshida,¹²⁵ H. Yum,⁷⁹ M. Yvert,³ A. Zadrożny,¹⁰¹ M. Zanolin,⁸⁷ J.-P. Zendri,¹²³ F. Zhang,¹¹ L. Zhang,¹ C. Zhao,⁴⁰ H. Zhu,⁸¹ X. J. Zhu,⁴⁰ N. Zotov,¹¹⁶ M. E. Zucker,¹¹ and J. Zweigig¹

(LIGO Scientific Collaboration and Virgo Collaboration)

- ¹LIGO—California Institute of Technology, Pasadena, California 91125, USA
²Louisiana State University, Baton Rouge, Louisiana 70803, USA
³Laboratoire d'Annecy-le-Vieux de Physique des Particules (LAPP), Université de Savoie, CNRS/IN2P3, F-74941 Annecy-le-Vieux, France
⁴Università di Salerno, Fisciano, I-84084 Salerno, Italy
⁵INFN, Sezione di Napoli, Complesso Universitario di Monte S. Angelo, I-80126 Napoli, Italy
⁶LIGO Livingston Observatory, Livingston, Louisiana 70754, USA
⁷Cardiff University, Cardiff CF24 3AA, United Kingdom
⁸University of Salerno, I-84084 Fisciano (Salerno), Italy and INFN, Sezione di Napoli, Complesso Universitario di Monte S. Angelo, I-80126 Napoli, Italy
⁹Albert-Einstein-Institut, Max-Planck-Institut für Gravitationsphysik, D-30167 Hannover, Germany
¹⁰Nikhef, Science Park, 1098 XG Amsterdam, The Netherlands
¹¹LIGO—Massachusetts Institute of Technology, Cambridge, Massachusetts 02139, USA
¹²Instituto Nacional de Pesquisas Espaciais, 12227-010 São José dos Campos, SP, Brazil
¹³University of Wisconsin—Milwaukee, Milwaukee, Wisconsin 53201, USA
¹⁴Leibniz Universität Hannover, D-30167 Hannover, Germany
¹⁵Università di Siena, I-53100 Siena, Italy
¹⁶INFN, Sezione di Pisa, I-56127 Pisa, Italy
¹⁷University of Florida, Gainesville, Florida 32611, USA
¹⁸The University of Mississippi, University, Mississippi 38677, USA
¹⁹California State University Fullerton, Fullerton, California 92831, USA
²⁰INFN, Sezione di Roma, I-00185 Roma, Italy
²¹University of Birmingham, Birmingham B15 2TT, United Kingdom
²²Albert-Einstein-Institut, Max-Planck-Institut für Gravitationsphysik, D-14476 Golm, Germany
²³Montana State University, Bozeman, Montana 59717, USA
²⁴European Gravitational Observatory (EGO), I-56021 Cascina, Pisa, Italy
²⁵Syracuse University, Syracuse, New York 13244, USA
²⁶LIGO Hanford Observatory, Richland, Washington 99352, USA
²⁷SUPA, University of Glasgow, Glasgow G12 8QQ, United Kingdom
²⁸APC, AstroParticule et Cosmologie, Université Paris Diderot, CNRS/IN2P3, CEA/Irfu, Observatoire de Paris, Sorbonne Paris Cité, 10, rue Alice Domon et Léonie Duquet, F-75205 Paris Cedex 13, France
²⁹Columbia University, New York, New York 10027, USA
³⁰Stanford University, Stanford, California 94305, USA
³¹Università di Pisa, I-56127 Pisa, Italy
³²CAMK-PAN, 00-716 Warsaw, Poland
³³Università degli Studi di Genova, I-16146 Genova, Italy
³⁴INFN, Sezione di Genova, I-16146 Genova, Italy
³⁵The University of Texas at Brownsville, Brownsville, Texas 78520, USA
³⁶San Jose State University, San Jose, California 95192, USA
³⁷Moscow State University, Moscow 119992, Russia
³⁸LAL, Université Paris—Sud, IN2P3/CNRS, F-91898 Orsay, France
³⁹NASA/Goddard Space Flight Center, Greenbelt, Maryland 20771, USA
⁴⁰University of Western Australia, Crawley, Western Australia 6009, Australia
⁴¹ARTEMIS, Université Nice-Sophia-Antipolis, CNRS and Observatoire de la Côte d'Azur, F-06304 Nice, France
⁴²Institut de Physique de Rennes, CNRS, Université de Rennes 1, F-35042 Rennes, France
⁴³Laboratoire des Matériaux Avancés (LMA), IN2P3/CNRS, Université de Lyon, F-69622 Villeurbanne, Lyon, France
⁴⁴Washington State University, Pullman, Washington 99164, USA
⁴⁵INFN, Sezione di Perugia, I-06123 Perugia, Italy
⁴⁶Università degli Studi di Urbino “Carlo Bo,” I-61029 Urbino, Italy
⁴⁷INFN, Sezione di Firenze, I-50019 Sesto Fiorentino, Firenze, Italy
⁴⁸University of Oregon, Eugene, Oregon 97403, USA
⁴⁹Laboratoire Kastler Brossel, ENS, CNRS, UPMC, Université Pierre et Marie Curie, F-75005 Paris, France
⁵⁰Astronomical Observatory Warsaw University, 00-478 Warsaw, Poland
⁵¹VU University Amsterdam, 1081 HV Amsterdam, The Netherlands
⁵²University of Maryland, College Park, Maryland 20742, USA
⁵³University of Massachusetts—Amherst, Amherst, Massachusetts 01003, USA

- ⁵⁴*Universitat de les Illes Balears, E-07122 Palma de Mallorca, Spain*
- ⁵⁵*Università di Napoli “Federico II,” Complesso Universitario di Monte Sant’Angelo, I-80126 Napoli, Italy*
- ⁵⁶*Canadian Institute for Theoretical Astrophysics, University of Toronto, Toronto, Ontario M5S 3H8, Canada*
- ⁵⁷*Tsinghua University, Beijing 100084, China*
- ⁵⁸*University of Michigan, Ann Arbor, Michigan 48109, USA*
- ⁵⁹*Rochester Institute of Technology, Rochester, New York 14623, USA*
- ⁶⁰*INFN, Sezione di Roma Tor Vergata, I-00133 Roma, Italy*
- ⁶¹*National Tsing Hua University, Hsinchu, Taiwan 300*
- ⁶²*Charles Sturt University, Wagga Wagga, New South Wales 2678, Australia*
- ⁶³*Caltech—CaRT, Pasadena, California 91125, USA*
- ⁶⁴*Pusan National University, Busan 609-735, Korea*
- ⁶⁵*Australian National University, Canberra, Australian Capital Territory 0200, Australia*
- ⁶⁶*Carleton College, Northfield, Minnesota 55057, USA*
- ⁶⁷*Università di Roma Tor Vergata, I-00133 Roma, Italy*
- ⁶⁸*Università di Roma “La Sapienza,” I-00185 Roma, Italy*
- ⁶⁹*The George Washington University, Washington, D.C. 20052, USA*
- ⁷⁰*University of Cambridge, Cambridge CB2 1TN, United Kingdom*
- ⁷¹*University of Minnesota, Minneapolis, Minnesota 55455, USA*
- ⁷²*The University of Sheffield, Sheffield S10 2TN, United Kingdom*
- ⁷³*Wigner RCP, RMKI, H-1121 Budapest, Konkoly Thege Miklós út 29-33, Hungary*
- ⁷⁴*University of Sannio at Benevento, I-82100 Benevento, Italy and INFN (Sezione di Napoli), I-80126 Napoli, Italy*
- ⁷⁵*Inter-University Centre for Astronomy and Astrophysics, Pune 411007, India*
- ⁷⁶*Università di Trento, I-38123 Povo, Trento, Italy*
- ⁷⁷*INFN, Gruppo Collegato di Trento, I-38050 Povo, Trento, Italy*
- ⁷⁸*California Institute of Technology, Pasadena, California 91125, USA*
- ⁷⁹*Northwestern University, Evanston, Illinois 60208, USA*
- ⁸⁰*Montclair State University, Montclair, New Jersey 07043, USA*
- ⁸¹*The Pennsylvania State University, University Park, Pennsylvania 16802, USA*
- ⁸²*MTA Eötvös University, “Lendulet” Astrophysics Research Group, Budapest 1117, Hungary*
- ⁸³*National Astronomical Observatory of Japan, Tokyo 181-8588, Japan*
- ⁸⁴*Università di Perugia, I-06123 Perugia, Italy*
- ⁸⁵*University of Szeged, Dóm tér 9, Szeged 6720, Hungary*
- ⁸⁶*Rutherford Appleton Laboratory, HSIC, Chilton, Didcot, Oxon OX11 0QX, United Kingdom*
- ⁸⁷*Embry-Riddle Aeronautical University, Prescott, Arizona 86301, USA*
- ⁸⁸*Perimeter Institute for Theoretical Physics, Ontario N2L 2Y5, Canada*
- ⁸⁹*American University, Washington, D.C. 20016, USA*
- ⁹⁰*College of William and Mary, Williamsburg, Virginia 23187, USA*
- ⁹¹*University of Adelaide, Adelaide, South Australia 5005, Australia*
- ⁹²*Raman Research Institute, Bangalore, Karnataka 560080, India*
- ⁹³*Korea Institute of Science and Technology Information, Daejeon 305-806, Korea*
- ⁹⁴*University of Białystok, 15-424 Białystok, Poland*
- ⁹⁵*University of Southampton, Southampton SO17 1BJ, United Kingdom*
- ⁹⁶*IISER-TVM, CET Campus, Trivandrum Kerala 695016, India*
- ⁹⁷*Hobart and William Smith Colleges, Geneva, New York 14456, USA*
- ⁹⁸*Institute of Applied Physics, Nizhny Novgorod 603950, Russia*
- ⁹⁹*Seoul National University, Seoul 151-742, Korea*
- ¹⁰⁰*Hanyang University, Seoul 133-791, Korea*
- ¹⁰¹*NCBJ, 05-400 Świerk-Otwock, Poland*
- ¹⁰²*IM-PAN, 00-956 Warsaw, Poland*
- ¹⁰³*Institute for Plasma Research, Bhat, Gandhinagar 382428, India*
- ¹⁰⁴*Utah State University, Logan, Utah 84322, USA*
- ¹⁰⁵*The University of Melbourne, Parkville, Victoria 3010, Australia*
- ¹⁰⁶*University of Brussels, Brussels 1050, Belgium*
- ¹⁰⁷*SUPA, University of Strathclyde, Glasgow G1 1XQ, United Kingdom*
- ¹⁰⁸*ESPCI, CNRS, F-75005 Paris, France*
- ¹⁰⁹*Università di Camerino, Dipartimento di Fisica, I-62032 Camerino, Italy*
- ¹¹⁰*The University of Texas at Austin, Austin, Texas 78712, USA*

- ¹¹¹*Southern University and A&M College, Baton Rouge, Louisiana 70813, USA*
¹¹²*IISER-Kolkata, Mohanpur, West Bengal 741252, India*
¹¹³*National Institute for Mathematical Sciences, Daejeon 305-390, Korea*
¹¹⁴*RRCAT, Indore, MP 452013, India*
¹¹⁵*Tata Institute for Fundamental Research, Mumbai 400005, India*
¹¹⁶*Louisiana Tech University, Ruston, Louisiana 71272, USA*
¹¹⁷*SUPA, University of the West of Scotland, Paisley PA1 2BE, United Kingdom*
¹¹⁸*Institute of Astronomy, 65-265 Zielona Góra, Poland*
¹¹⁹*Indian Institute of Technology, Gandhinagar, Ahmedabad, Gujarat 382424, India*
¹²⁰*Department of Astrophysics/IMAPP, Radboud University Nijmegen, P.O. Box 9010, 6500 GL Nijmegen, The Netherlands*
¹²¹*Andrews University, Berrien Springs, Michigan 49104, USA*
¹²²*Trinity University, San Antonio, Texas 78212, USA*
¹²³*INFN, Sezione di Padova, I-35131 Padova, Italy*
¹²⁴*University of Washington, Seattle, Washington 98195, USA*
¹²⁵*Southeastern Louisiana University, Hammond, Louisiana 70402, USA*
¹²⁶*Abilene Christian University, Abilene, Texas 79699, USA*
- (Received 4 November 2014; published 8 January 2015)

Searches for a stochastic gravitational-wave background (SGWB) using terrestrial detectors typically involve cross-correlating data from pairs of detectors. The sensitivity of such cross-correlation analyses depends, among other things, on the separation between the two detectors: the smaller the separation, the better the sensitivity. Hence, a colocated detector pair is more sensitive to a gravitational-wave background than a noncolocated detector pair. However, colocated detectors are also expected to suffer from correlated noise from instrumental and environmental effects that could contaminate the measurement of the background. Hence, methods to identify and mitigate the effects of correlated noise are necessary to achieve the potential increase in sensitivity of colocated detectors. Here we report on the first SGWB analysis using the two LIGO Hanford detectors and address the complications arising from correlated environmental noise. We apply correlated noise identification and mitigation techniques to data taken by the two LIGO Hanford detectors, H1 and H2, during LIGO's fifth science run. At low frequencies, 40–460 Hz, we are unable to sufficiently mitigate the correlated noise to a level where we may confidently measure or bound the stochastic gravitational-wave signal. However, at high frequencies, 460–1000 Hz, these techniques are sufficient to set a 95% confidence level upper limit on the gravitational-wave energy density of $\Omega(f) < 7.7 \times 10^{-4} (f/900 \text{ Hz})^3$, which improves on the previous upper limit by a factor of ~ 180 . In doing so, we demonstrate techniques that will be useful for future searches using advanced detectors, where correlated noise (e.g., from global magnetic fields) may affect even widely separated detectors.

DOI: [10.1103/PhysRevD.91.022003](https://doi.org/10.1103/PhysRevD.91.022003)

PACS numbers: 95.85.Sz, 04.80.Nn, 07.05.Kf, 97.60.Jd

I. INTRODUCTION

The detection of a stochastic gravitational-wave background (SGWB), of either cosmological or astrophysical origin, is a major science goal for both current and planned searches for gravitational waves (GWs) [1–4]. Given the weakness of the gravitational interaction, cosmological GWs are expected to decouple from matter in the early Universe much earlier than any other form of radiation (e.g., photons, neutrinos, etc.). The detection of such a primordial GW background by the current ground-based detectors [5–7], proposed space-based detectors [8,9], or a pulsar timing array [10,11] would give us a picture of the Universe mere fractions of a second after the big bang [1–3,12], allowing us to study the physics of the highest

energy scales, unachievable in standard laboratory experiments [4]. The recent results from the BICEP2 experiment indicate the existence of cosmic microwave background (CMB) *B*-mode polarization at degree angular scales [13], which may be due to an ultralow frequency primordial GW background, such as would be generated by amplification of vacuum fluctuations during cosmological inflation; however, it cannot currently be ruled out that the observed *B*-mode polarization is due to a Galactic dust foreground [14,15]. These GWs and their high-frequency counterparts in the standard slow-roll inflationary model are several orders of magnitude below the sensitivity levels of current and advanced LIGO detectors. Hence they are not the target of our current analysis. However, many nonstandard inflationary models predict GWs that could be detected by advanced LIGO detectors.

*shivaraj.kandhasamy@ligo.org

On the other hand, the detection of a SGWB due to spatially and temporally unresolved foreground astrophysical sources such as magnetars [16], rotating neutron stars [17], galactic and extragalactic compact binaries [18–20], or the inspiral and collisions of supermassive black holes associated with distant galaxy mergers [21] would provide information about the spatial distribution and formation rate of these various source populations.

Given the random nature of a SGWB, searches require cross-correlating data from two or more detectors [1,22–25], under the assumption that correlated noise between any two detectors is negligible. For such a case, the contribution to the cross-correlation from the (common) GW signal grows linearly with the observation time T , while that from the noise grows like \sqrt{T} . Thus, the signal-to-noise ratio (SNR) also grows like \sqrt{T} . This allows one to search for stochastic signals buried within the detector noise by integrating for a sufficiently long interval of time.

For the widely separated detectors in Livingston, Louisiana, and Hanford, Washington, the physical separation (~ 3000 km) eliminates the coupling of local instrumental and environmental noise between the two detectors, while global disturbances such as electromagnetic resonances are at a sufficiently low level that they are not observable in coherence measurements between the (first-generation) detectors at their design sensitivity [5,26–30].

While physically separated detectors have the advantage of reduced correlated noise, they have the disadvantage of reduced sensitivity to a SGWB; physically separated detectors respond at different times to GWs from different directions and with differing response amplitudes depending on the relative orientation and (mis)alignment of the detectors [23–25]. Colocated and coaligned detectors, on the other hand, such as the 4 km and 2 km interferometers in Hanford, Washington (denoted H1 and H2), respond identically to GWs from all directions and for all frequencies below a few kHz. They are thus, potentially, an order of magnitude more sensitive to a SGWB than e.g., the Hanford-Livingston LIGO pair. But this potential gain in sensitivity can be offset by the presence of correlated instrumental and environmental noise, given that the two detectors share the same local environment. Methods to identify and mitigate the effects of correlated noise are thus needed to realize the potential increase in sensitivity of colocated detectors.

In this paper, we apply several noise identification and mitigation techniques to data taken by the two LIGO Hanford detectors, H1 and H2, during LIGO’s fifth science run (S5, November 4, 2005, to September 30, 2007) in the context of a search for a SGWB. This is the first stochastic analysis using LIGO science data that addresses the complications introduced by correlated environmental noise. As discussed in Refs. [29,30], the coupling of global magnetic fields to noncolocated advanced LIGO detectors

could produce significant correlations between them thereby reducing their sensitivity to SGWB by an order of magnitude. We expect the current H1-H2 analysis to provide a useful precedent for SGWB searches with advanced detectors in such an (expected) correlated noise environment.

Results are presented at different stages of cleaning applied to the data. We split the analysis into two parts—one for the frequency band 460–1000 Hz, where we are able to successfully identify and exclude significant narrow-band correlations; and the other for the band 80–160 Hz, where even after applying the noise reduction methods there is still evidence of residual contamination, resulting in a large systematic uncertainty for this band. The frequencies below 80 Hz and between 160–460 Hz are not included in the analysis because of poor detector sensitivity and contamination by known noise artifacts. We observe no evidence of a SGWB and so our final results are given in the form of upper limits. Due to the presence of residual correlated noise between 80–160 Hz, we do not set any upper limit for this frequency band. Since we do not observe any such residual noise between 460–1000 Hz, in that frequency band and the five subbands assigned to it, we set astrophysical upper limits on the energy density of stochastic GWs.

The rest of the paper is organized as follows. In Sec. II, we describe sources of correlated noise in H1 and H2, and the environmental and instrumental monitoring system. In Sec. III we describe the cross-correlation procedure used to search for a SGWB. In Secs. IV and V we describe the methods that we used to identify correlated noise, and the steps that we took to mitigate it. In Secs. VI and VII we give the results of our analysis applied to the S5 H1-H2 data. Finally, in Sec. VIII we summarize our results and discuss potential improvements to the methods discussed in this paper.

II. COMMON NOISE IN THE TWO LIGO HANFORD DETECTORS

At each of the LIGO observatory sites the detectors are supplemented with a set of sensors to monitor the local environment [5,31]. Seismometers and accelerometers measure vibrations of the ground and various detector components; microphones monitor acoustic noise; magnetometers monitor magnetic fields that could couple to the test masses (end mirrors of the interferometers) via the magnets attached to the test masses to control their positions; radio receivers monitor radio frequency (RF) power around the laser modulation frequencies, and voltage line monitors record fluctuations in the ac power. These physical environment monitoring (PEM) channels are used to detect instrumental and environmental disturbances that can couple to the GW strain channel. We assume that these channels are completely insensitive to GW strain. The PEM channels are placed at strategic locations around the

observatory, especially near the corner and ends of the L-shaped interferometer where important laser, optical, and suspension systems reside in addition to the test masses themselves.

Information provided by the PEM channels is used in many different ways. The most basic application is the creation of numerous *data quality flags* identifying stretches of data that are corrupted by instrumental or environmental noise [32]. The signals from PEM channels are critical in defining these flags; microphones register airplanes flying overhead, seismometers and accelerometers detect elevated seismic activity or anthropogenic events (trucks, trains, logging), and magnetometers detect fluctuations in the mains power supply and the Earth's magnetic field.

In searches for transient GW signals, such as burst or coalescing binary events, information from the PEM channels has been used to construct *vetoos* [33–36]. When a clear association can be made between a measured environmental event and a coincident *glitch* in the output channel of the detector, then these times are excluded from the transient GW searches. These event-by-event vetoos exclude times of order hundreds of milliseconds to a few seconds.

Similarly, noise at specific frequencies, called *noise lines*, can affect searches for GWs from rotating neutron stars or even for a SGWB. In S5, data from PEM channels were used to verify that some of the apparent periodic signals were in fact due to noise sources at the observatories [37,38]. Typically the neutron-star search algorithms can also be applied to the PEM data to find channels that have noise lines at the same frequencies as those in the detector output channel. The coherence is also calculated between the detector output and the PEM channels, and these results provide additional information for determining the source of noise lines.

The study of noise lines has also benefited past LIGO searches for stochastic GWs. For example, in LIGO's search for a SGWB using the data from the S4 run [27], correlated noise between the Hanford and Livingston detectors was observed in the form of a forest of sharp 1 Hz harmonic lines. It was subsequently determined that these lines were caused by the sharp ramp of a one-pulse-per-second signal, injected into the data acquisition system to synchronize it with the Global Positioning System (GPS) time reference. In the S5 stochastic search [28], there were other prominent noise lines that were subsequently identified through the use of the PEM signals.

In addition to *passive* studies, where the PEM signals are observed and associations are made to detector noise, there have also been a series of *active* investigations where noise was injected into the detector environment in order to measure its coupling to the GW channel. Acoustic, seismic, magnetic, and RF electromagnetic noise were injected into the observatory environment at various locations and

responses of the detectors were studied. These tests provided clues and ways to better isolate the detectors from the environment.

All the previous LIGO searches for a SGWB have used the physically separated Hanford and Livingston detectors and assumed that common noise between these noncolocated detectors was inconsequential. This assumption was strongly supported by observations—i.e., none of the coherence measurements performed to date between these detectors revealed the presence of correlations other than those known to be introduced by the instrument itself (for example, harmonics of the 60 Hz power line). Since the analysis presented here uses the two colocated Hanford detectors, which are susceptible to correlated noise due to the local environment, new methods were required to identify and mitigate the correlated noise.

III. CROSS-CORRELATION PROCEDURE

The energy density spectrum of SGWB is defined as

$$\Omega_{\text{gw}}(f) \equiv \frac{f}{\rho_c} \frac{d\rho_{\text{gw}}}{df}, \quad (1)$$

where $\rho_c (= \frac{3c^2 H_0^2}{8\pi G})$ is the critical energy density and ρ_{gw} is the GW energy density contained in the frequency range f and $f + df$. Since most theoretical models of stochastic backgrounds in the LIGO band are characterized by a power-law spectrum, we will assume that the fractional energy density in GWs [39] has the form

$$\Omega_{\text{gw}}(f) = \Omega_\alpha \left(\frac{f}{f_{\text{ref}}} \right)^\alpha, \quad (2)$$

where α is the spectral index and f_{ref} is some reference frequency. We will consider two values for the spectral index: $\alpha = 0$ which is representative of many cosmological models, and $\alpha = 3$ which is characteristic of many astrophysical models. This latter case corresponds to a flat (i.e., constant) one-sided power spectral density (PSD) in the strain output of a detector $S_{\text{gw}}(f)$, since

$$S_{\text{gw}}(f) = \frac{3H_0^2}{10\pi^2} \frac{\Omega_{\text{gw}}(f)}{f^3} \propto f^{\alpha-3}. \quad (3)$$

Here H_0 is the present value of the Hubble parameter, assumed to be $H_0 = 68$ km/s/Mpc [40].

Following the procedures described in [25], we construct our cross-correlation statistic as estimators of Ω_α for *individual* frequency bins, of width Δf , centered at each (positive) frequency f . These estimators are simply the measured values of the cross spectrum of the strain output of two detectors divided by the expected shape of the cross-correlation due to a GW background with spectral index α :

$$\hat{\Omega}_\alpha(f) \equiv \frac{2}{T} \frac{\Re[\tilde{s}_1^*(f)\tilde{s}_2(f)]}{\gamma(f)S_\alpha(f)}. \quad (4)$$

Here T is the duration of the data segments used for Fourier transforms; $\tilde{s}_1(f)$, $\tilde{s}_2(f)$ are the Fourier transforms of the strain time series in the two detectors; $S_\alpha(f)$ is proportional to the assumed spectral shape,

$$S_\alpha(f) \equiv \frac{3H_0^2}{10\pi^2} \frac{1}{f^3} \left(\frac{f}{f_{\text{ref}}}\right)^\alpha; \quad (5)$$

and $\gamma(f)$ is the overlap reduction function [23–25], which encodes the reduction in sensitivity due to the separation and relative alignment of the two detectors. For the H1-H2 detector pair, $\gamma(f) \approx 1$ for all frequencies below a few kHz [41].

In the absence of correlated noise, one can show that the above estimators are *optimal*—i.e., they are unbiased, minimal-variance estimators of Ω_α for stochastic background signals with spectral index α . Assuming that the detector noise is Gaussian, stationary, and much larger in magnitude than the GW signal, the expectation value of the variance of the estimators is given by

$$\sigma_{\hat{\Omega}_\alpha}^2(f) \approx \frac{1}{2T\Delta f} \frac{P_1(f)P_2(f)}{\gamma^2(f)S_\alpha^2(f)}, \quad (6)$$

where $P_1(f)$, $P_2(f)$ are the one-sided PSDs of the detector output $\tilde{s}_1(f)$, $\tilde{s}_2(f)$ respectively. For a frequency band consisting of several bins of width Δf , the optimal estimator and corresponding variance are given by the weighted sum

$$\hat{\Omega}_\alpha \equiv \frac{\sum_f \sigma_{\hat{\Omega}_\alpha}^{-2}(f) \hat{\Omega}_\alpha(f)}{\sum_{f'} \sigma_{\hat{\Omega}_\alpha}^{-2}(f')}, \quad \sigma_{\hat{\Omega}_\alpha}^{-2} \equiv \sum_f \sigma_{\hat{\Omega}_\alpha}^{-2}(f). \quad (7)$$

A similar weighted sum can be used to optimally combine the estimators calculated for different time intervals [42].

In the presence of correlated noise, the estimators are biased. The expected values are then

$$\langle \hat{\Omega}_\alpha(f) \rangle = \Omega_\alpha + \eta_\alpha(f), \quad (8)$$

where

$$\eta_\alpha(f) \equiv \frac{\Re[N_{12}(f)]}{\gamma(f)S_\alpha(f)}. \quad (9)$$

Here $N_{12}(f) \equiv \frac{2}{T} \langle \tilde{n}_1^*(f)\tilde{n}_2(f) \rangle$ is the one-sided cross-spectral density (CSD) of the correlated noise contribution \tilde{n}_1 , \tilde{n}_2 to \tilde{s}_1 , \tilde{s}_2 . The expression for the variance $\sigma_{\hat{\Omega}_\alpha}^2(f)$ is unchanged in the presence of correlated noise provided $|N_{12}(f)| \ll P_1(f), P_2(f)$. For the summed estimator $\hat{\Omega}_\alpha$, we have

$$\langle \hat{\Omega}_\alpha \rangle = \Omega_\alpha + \eta_\alpha, \quad (10)$$

where

$$\eta_\alpha \equiv \frac{\sum_f \sigma_{\hat{\Omega}_\alpha}^{-2}(f) \eta_\alpha(f)}{\sum_{f'} \sigma_{\hat{\Omega}_\alpha}^{-2}(f')} \quad (11)$$

is the contribution from correlated noise averaged over time (not shown) and frequency. Thus, *correlated noise biases our estimates of the amplitude of a SGWB*. Here we also note that η_α can be positive or negative while Ω_α is positive by definition. The purpose of the noise identification and removal methods that we describe below is to reduce this bias as much as possible.

IV. METHODS FOR IDENTIFYING CORRELATED NOISE

A. Coherence calculation

Perhaps the simplest method for identifying correlated noise in the H1-H2 data is to calculate the magnitude squared coherence, $\hat{\Gamma}_{12}(f) \equiv |\gamma_{12}(f)|^2$, where

$$\gamma_{12}(f) \equiv \frac{2}{T} \frac{\langle \tilde{s}_1^*(f)\tilde{s}_2(f) \rangle_N}{\sqrt{\langle P_1(f) \rangle_N \langle P_2(f) \rangle_N}}. \quad (12)$$

Here T denotes the duration of a single segment of data, and angle brackets $\langle \rangle_N$ denote an average over N segments used to estimate the CSD and PSDs that enter the expression for γ_{12} . If there are no correlations (either due to noise or a GW signal) in the data, the expected value of $\hat{\Gamma}_{12}(f)$ is equal to $1/N$. This method is especially useful at finding narrow-band features that stick out above the expected $1/N$ level. Since we expect a SGWB to be broadband, with relatively little variation in the LIGO band (~ 80 – 1000 Hz), most of these features can be attributed to instrumental and/or environmental correlations. We further investigate these lines with data from other PEM channels and once we confirm that they are indeed environmental/instrumental artifacts, we remove them from our analysis.

Plots of $\hat{\Gamma}_{12}(f)$ for three different frequency resolutions are shown in Figs. 1 and 2 for two frequency bands, 80–160 Hz and 460–1000 Hz, respectively. In Fig. 1, note the relatively wide structure around 120 Hz, which is especially prominent in the bottom panel where the frequency resolution is 100 mHz. This structure arises from low-frequency noise (dominated by seismic and other mechanical noise) up-converting to frequencies around the 60 Hz harmonics via a bilinear coupling mechanism. While these coupling mechanisms are not fully understood, we reject the band from 102–126 Hz for our analysis, given the elevated correlated noise seen in this band. (A similar plot at slightly lower and higher frequencies shows similar noisy bands from 40–80 Hz and 160–200 Hz.) A closer look at the coherence also identifies smaller structures at

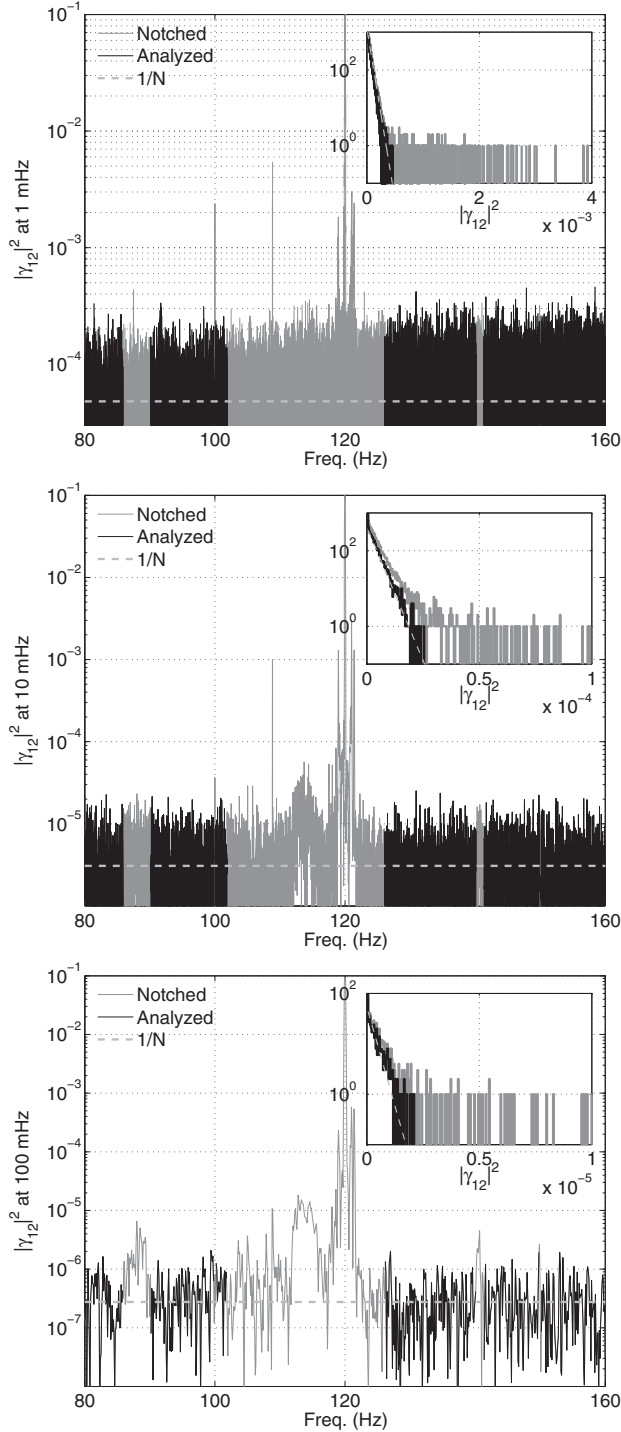


FIG. 1. Coherence $\hat{\Gamma}_{12}$ between H1 and H2 computed in the frequency band 80–160 Hz using all of the S5 data, for three different frequency resolutions: 1 mHz, 10 mHz, and 100 mHz (from top panel to bottom). The insets show that the histograms of the coherence at the analyzed frequencies follow the expected exponential distribution for Gaussian noise, as well as the presence of a long tail of high coherence values at notched frequencies. A stochastic broadband GW signal of SNR = 5 would appear at a level of $\lesssim 10 \times$ below the dashed $1/N$ line.

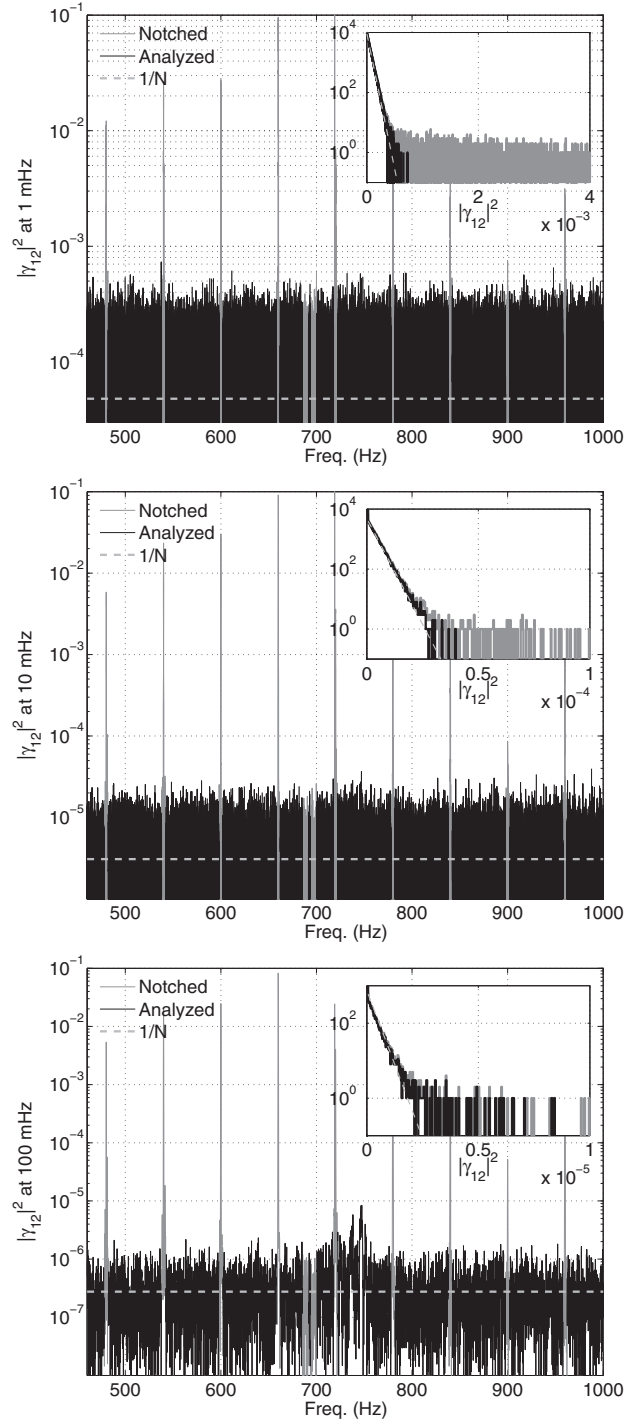


FIG. 2. Same as Fig. 1 but at higher frequencies, 460–1000 Hz. Note the coherence peaks at the harmonics of the 60 Hz power lines (notched in the analysis). The elevated coherence near 750 Hz at 100 mHz resolution is due to acoustic noise coupling to the GW channels. The long tail in the 100 mHz plot is due to excess noise around 750 Hz, which was removed from the final analysis using PEM notchings (see Sec. V). A stochastic broadband GW signal of SNR = 5 would appear at a level of $\lesssim 10 \times$ below the dashed $1/N$ line.

86–90 Hz, 100 Hz, 140–141 Hz, and 150 Hz. A follow-up analysis of PEM channels (which is discussed in more detail later) revealed that the grayed bands in Figs. 1 and 2 were highly contaminated with acoustic noise or by low-frequency seismic noise up-converting to frequencies around the 60 Hz harmonics via a bilinear coupling mechanism; so we rejected these frequency bands from subsequent analysis. As mentioned earlier, the 160–460 Hz band was not used in this analysis, because of similar acoustic and seismic contamination, as well as violin-mode resonances of the mirror-suspension wires (see Sec. IV D).

As shown in Fig. 2, the coherence at high frequencies (460–1000 Hz) is relatively clean. The only evidence of narrow-band correlated noise is in ± 2 Hz bands around the 60 Hz power-line harmonics, and violin-mode resonances of mirror suspensions at 688.5 ± 2.8 Hz and 697 ± 3.1 Hz. The elevated coherence near 750 Hz at 100 mHz resolution is due to acoustic noise coupling to the GW channels. Notching the power-line harmonics and violin-mode resonances amounts to the removal of $\sim 9\%$ of the frequency bins over the entire high-frequency band.

B. Time-shift analysis

A second method for identifying narrow-band correlated noise is to *time shift* the time-series output of one detector relative to that of the other detector before doing the cross-correlation analysis [43]. By introducing a shift of ± 1 second, which is significantly larger than the correlation time for a broadband GW signal (~ 10 ms, cf. Fig. 9), we eliminate broadband GW correlations while preserving narrow-band noise features. Using segments of duration $T = 1$ s, we calculate the time-shifted estimators $\hat{\Omega}_{\alpha, \text{TS}}(f)$, variance $\sigma_{\hat{\Omega}_{\alpha, \text{TS}}}^2(f)$, and their ratio $\text{SNR}_{\hat{\Omega}_{\alpha, \text{TS}}}(f) \equiv \hat{\Omega}_{\alpha, \text{TS}}(f) / \sigma_{\hat{\Omega}_{\alpha, \text{TS}}}(f)$. The calibration and conditioning of the data is performed in exactly the same way as for the final search, which is described in detail in Secs. V and VI.

We excise any frequency bin with $|\text{SNR}_{\hat{\Omega}_{\alpha, \text{TS}}}(f)| > 2$ on the grounds that it is likely contaminated by correlated noise. This threshold was chosen on the basis of initial studies performed using playground data to understand the effectiveness of such a cut. This criterion can be checked for different time scales, such as weeks, months, or the entire data set. This allows us to identify transient effects on different time scales, which may be diluted (and unobservable) when averaged over the entire data set.

C. PEM coherence calculations

Another method for identifying correlated noise is to first try to identify the noise sources that couple into the individual detector outputs by calculating the coherence of \tilde{s}_1 and \tilde{s}_2 with various PEM channels \tilde{z}_I :

$$\hat{\gamma}_{iI}(f) \equiv \frac{2}{T} \frac{\langle \tilde{s}_i^*(f) \tilde{z}_I(f) \rangle_N}{\sqrt{\langle P_i(f) \rangle_N \langle P_I(f) \rangle_N}}. \quad (13)$$

Here $i = 1, 2$ labels the detector outputs and I labels the PEM channels. For our analysis we used 172 PEM channels located near the two detectors. In addition to the PEM channels, we used a couple of auxiliary channels associated with the stabilization of the frequency of the lasers used in the detectors, which potentially carry information about instrumental correlations between the two detectors. (Hereafter, the usage of the acronym PEM will also include these two auxiliary channels.) The Fourier transforms are calculated for each minute of data ($T = 60$ s), and the average CSDs and PSDs are computed for extended time periods—weeks, months, or the entire run. We then perform the following maximization over all PEM channels, for each frequency bin f , defining

$$\hat{\gamma}_{12, \text{PEM}}(f) \equiv \max_I \Re[\hat{\gamma}_{1I}(f) \times \hat{\gamma}_{2I}^*(f)]. \quad (14)$$

Note that by construction $\hat{\gamma}_{12, \text{PEM}}(f)$ is real.

As discussed in [44], $\hat{\gamma}_{12, \text{PEM}}(f)$ is an estimate of the instrumental or environmental contribution to the coherence between the GW channels of H1 and H2. This estimate is only approximate, however, and potentially suffers from systematic errors for a few reasons. First, the PEM coverage of the observatory may be incomplete—i.e., there may be environmental or instrumental effects that are not captured by the existing array of PEMs. Second, some of the PEM channels may be correlated. Hence, a rigorous approach would require calculating a matrix of elements $\hat{\gamma}_{IJ}(f)$, and then inverting this matrix or solving a set of linear equations involving elements of $\hat{\gamma}_{IJ}(f)$. In practice, due to the large number of channels and the large amount of data, this is a formidable task. Instead, we simply maximize, frequency by frequency, over the contributions from different PEM channels and use this maximum as an estimate of the overall environmental contribution to $\hat{\gamma}_{12}(f)$. Finally, these coherence methods do not take into account the nonlinear up-conversion processes in which low-frequency disturbances, primarily seismic activity, excite higher-frequency modes in the instrument.

Since the measured signal-to-noise ratio for the estimator $\hat{\Omega}_{\alpha}(f)$ can be written as

$$\text{SNR}(f) = \sqrt{2T\Delta f} \Re[\hat{\gamma}_{12}(f)], \quad (15)$$

we can simply approximate the contribution of the PEM channels to the stochastic GW signal-to-noise ratio as

$$\text{SNR}_{\text{PEM}}(f) \equiv \sqrt{2T\Delta f} \hat{\gamma}_{12, \text{PEM}}(f), \quad (16)$$

remembering that $\hat{\gamma}_{12, \text{PEM}}(f)$ is real. The PEM contribution to the estimators $\hat{\Omega}_{\alpha}(f)$ is then

$$\hat{\Omega}_{\alpha, \text{PEM}}(f) \equiv \text{SNR}_{\text{PEM}}(f) \sigma_{\hat{\Omega}_{\alpha}}(f), \quad (17)$$

where $\sigma_{\hat{\Omega}_{\alpha}}(f)$ is the statistical uncertainty defined by Eq. (6).

We can use the PEM coherence calculations in two complementary ways. First, we can identify frequency bins with particularly large instrumental or environmental contributions by placing a threshold on $|\text{SNR}_{\text{PEM}}(f)|$ and exclude them from the analysis. Second, the frequency bins that pass this data-quality cut may still contain some residual environmental contamination. We can estimate at least part of this residual contamination by using $\hat{\Omega}_{\alpha, \text{PEM}}(f)$ for the remaining frequency bins.

As part of the analysis procedure, we were able to identify the PEM channels that were responsible for the largest coherent noise between the GW channels in H1 and H2 for each frequency bin. For both the low- and high-frequency analyses, microphones and accelerometers in the central building near the beam splitters of each interferometer registered the most significant noise. Within approximately 1 Hz of the 60 Hz harmonics, magnetometers and voltage line monitors registered the largest correlated noise, but these frequencies were already removed from the analysis due to the significant coherence (noise) level at these frequencies, as mentioned in Sec. IV A.

D. Comparing PEM-coherence and time-shift methods

Figure 3 shows a comparison of the SNRs calculated by the PEM-coherence and time-shift methods. The agreement between these two very different techniques in identifying

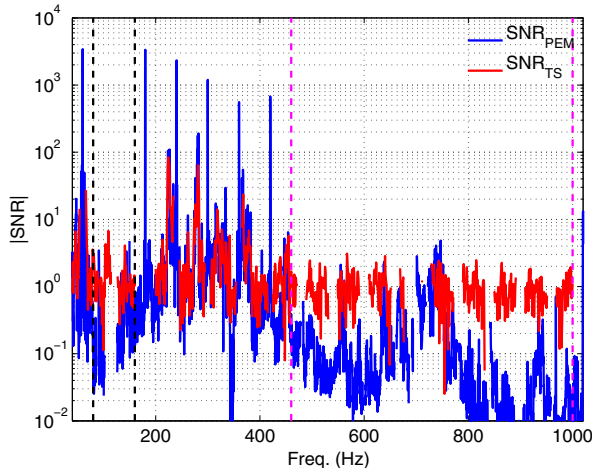


FIG. 3 (color online). Comparison of the (absolute value of the) SNRs calculated by the PEM-coherence and time-shift techniques. The vertical dotted lines indicate the frequency bands used for the low- (80–160 Hz; black dotted lines) and high-frequency (460–1000 Hz; magenta dotted lines) analyses. Note that $\text{SNR}_{\Omega_{\alpha, \text{TS}}}(f)$ is a true signal-to-noise ratio, so values $\lesssim 2$ are dominated by random statistical fluctuations. $\text{SNR}_{\Omega_{\alpha, \text{PEM}}}(f)$, on the other hand, is an estimate of the PEM contribution to the signal-to-noise ratio, so values even much lower than 2 are meaningful measurements (i.e., they are not statistical fluctuations). The two methods agree very well in identifying contaminated frequency bins or bands. Note that both methods indicate that the 80–160 Hz and 460–1000 Hz bands have relatively low levels of contamination.

contaminated frequency bins (those with $|\text{SNR}| \gtrsim$ a few) is remarkably good, which is an indication of their robustness and effectiveness. Moreover, Fig. 3 shows that the frequency region between 200 Hz and 460 Hz is particularly contaminated by environmental and/or instrumental effects. Hence, in this analysis we focus on the low-frequency region (80–160 Hz) which is the most sensitive to cosmological backgrounds (i.e., spectral index $\alpha = 0$), and on the high-frequency region (460–1000 Hz) which is less contaminated and more suitable for searches for astrophysically generated backgrounds (e.g., $\alpha = 3$).

We emphasize that the PEM channels only monitor the instrument and the environment, and are not sensitive to GWs. Similarly, the time-shift analysis, with a time shift of ± 1 second, is insensitive to broadband GW signals. Hence, any data-quality cuts based on the PEM and time-shift studies will not affect the astrophysical signatures in the data—i.e., they do not bias our estimates of the amplitude of a SGWB.

E. Other potential nonastrophysical sources of correlation

We note that any correlations that are produced by environmental signals that are not detected by the PEM sensors will not be detected by the PEM-coherence technique. Furthermore, if such correlations, or correlations from a nonenvironmental source, are broadband and flat (i.e., do not vary with frequency over our band), they will not be detected by either the PEM-coherence or the time-shift method. One potential source of broadband correlation between the two GW channels is the data acquisition system itself. We investigated this possibility by looking for correlations between 153 channel pairs that had no physical reason to be correlated. We found no broadband correlations, although we did find an unexplained narrow-band correlation at 281.5 Hz between 10 of 153 channel pairs. Note that 281.5 Hz is outside of the frequency bands analyzed in this study.

We addressed the potential of correlations from unmonitored environmental signals by searching for coupling sites four times over the course of the run by injecting large but localized acoustic, seismic, magnetic, and RF signals. New sensors were installed at the two coupling sites that had the least coverage. However, we found that the new sensors, even after scaling up to the full analysis period, contribute less than 1% of the total frequency notches; hence it is safe to assume that we had sufficient PEM coverage throughout our analysis period.

We also examined the possibility of correlations between the H1 and H2 detectors being generated by scattered light. We considered two mechanisms: first, light scattered from one detector affecting the other detector, and second, light from both detectors scattering off of the same site and returning to the originating detectors. We did not observe, and do not expect to observe, the first mechanism because

the frequencies of the two lasers, while very stable, may differ by gigahertz. If light from one interferometer scatters into the main beam of the other, it will likely be at a very different frequency and will not produce signals in our 8 kHz band when it beats against the reference light for that interferometer.

Nevertheless, we checked for a correlation produced by light from one detector entering the other by looking for the calibration signals [5] injected into one detector in the signal of the second detector. During S5, the following calibration line frequencies were injected into H1 and H2: 46.70 Hz, 393.10 Hz, 1144.30 Hz (H1) and 54.10 Hz, 407.30 Hz, 1159.7 Hz (H2). We note here that all those frequencies are outside of our analysis bands. We observed no correlation beyond the statistical error of the measurement at any of the three calibration line frequencies for either of the two detectors. This check was done for every week and month and for the entire S5 data set. Hence, we conclude that potential signals carried by the light in one detector are not coupled into the other detector.

In contrast, we have observed the second scattering mechanism, in which scattered light from the H1 beam returns to the H1 main beam and H2 light returns to the H2 main beam. This type of scattering can produce H1-H2 coupling if scattered light from H1 and from H2 both reflect off of the same vibrating surface (which modulates the length of the scattering paths) before recombining with their original main beams. This mechanism is thought to account for the observation that shaking the reflective end cap of the 4 km beam tube (just beyond an H1 end test mass) produced a shaking-frequency peak in both H1 and H2 GW channels, even though the nearest H2 component was 2 km away. However, this scattering mechanism is covered by the PEM system since the vibrations that modulate the beam path originate in the monitored environment.

We tested our expectation that scattering-induced correlations would be identified by our PEM-coherence method. We initiated a program to identify the most important scattering sites by mounting shakers on the vacuum system at 21 different locations that were selected as potential scattering sites, and searching for the shaking signal in the GW channels. All significant scattering sites that we found in this way were well monitored by the PEM system. At the site that produced the greatest coherence between the two detectors (a reflective flange close to and perpendicular to the beam paths of both interferometers), we mounted an accelerometer and found that the coherence between this accelerometer and the two GW channels was no greater than that for the sensors in the preexisting sensor system. These results suggest that the PEM system adequately monitored scattering coupling. As we shall show in Sec. VI A below, no correlated noise (either environmental or instrumental, either narrow band or broadband) that is not adequately covered by the PEM system is identified in the high-frequency analysis, further solidifying the adequacy of PEM system.

V. ANALYSIS PROCEDURE

In the previous section we described a number of methods for identifying correlated noise when searching for a SGWB. Here we enumerate the steps for selecting the time segments and frequency bands that were subsequently used for the analysis.

Step 1: We begin by selecting time periods that pass a number of data-quality flags. In particular, we reject periods when (i) there are problems with the calibration of the data; (ii) the interferometers are within 30 s of loss of servo control; (iii) there are artificial signals inserted into the data for calibration and characterization purposes; (iv) there are PEM noise injections; (v) various data acquisition overflows are observed; or (vi) there is missing data. With these cuts, the intersection of the H1 and H2 analyzable time was ~ 462 days for the S5 run.

Step 2: After selecting suitable data segments, we make a first pass at determining the frequency bins to use in the analysis by calculating the overall coherence between the detector outputs as described in Sec. IV A. Excess coherence levels led us to reject the frequencies 86–90 Hz, 100 Hz, 102–126 Hz, 140.25–141.25 Hz, and 150 Hz in the low-frequency band (80–160 Hz), as well as ± 2 Hz around the 60 Hz power-line harmonics and the violin-mode resonances at 688.5 ± 2.8 Hz and 697 ± 3.1 Hz in the high-frequency band (460–1000 Hz). It also identified a period of about 17 days in June 2007 (between GPS times 866526322 and 867670285), during which the detector H2 suffered from excessive transient noise glitches. We reject that period from the analysis.

Step 3: We perform a search for transient excess power in the data using the wavelet-based Kleine Welle algorithm [45], which was originally designed for detecting GW bursts. This algorithm is applied to the output of both detectors, producing a list of triggers for each detector. We then search the two trigger lists and reject any segment that contains transients with a Kleine Welle significance larger than 50 in either of the two detectors. The value of 50 is a conservative threshold, chosen based on other studies done on the distribution of such triggers in S5 [32].

Step 4: Having determined the reasonably good frequency bands, we then calculate $\hat{\Omega}_\alpha$ and its uncertainty $\sigma_{\hat{\Omega}_\alpha}$ summed over the whole band, cf. Eq. (7). The purpose of this calculation is to perform another level of data quality selection in the time domain by identifying noisy segments of 60 s duration. It is similar to the nonstationarity cut used in the previous analyses [26–28,46] where we remove time segments whose $\sigma_{\hat{\Omega}_\alpha}$ differs, by a predetermined amount, from that calculated by averaging over two neighboring segments. Here we use a 20% threshold on the difference. The combination of the time-domain data quality cuts described in Steps 1–4 removed about 22% of the available S5 H1-H2 data.

Step 5: After identifying and rejecting noisy time segments and frequency bins using Steps 1–4, we then use the

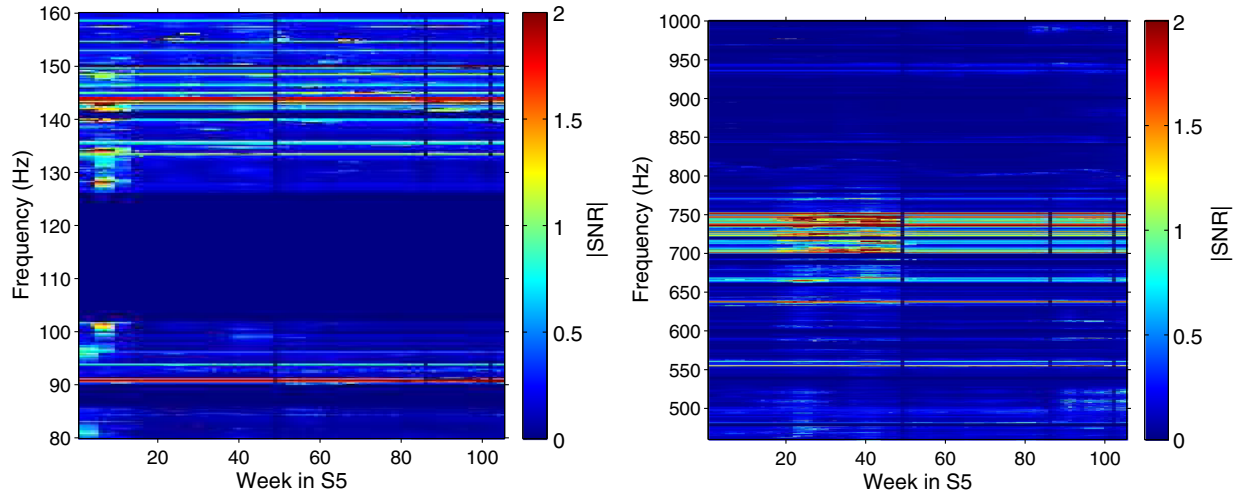


FIG. 4 (color online). Spectrograms displaying the absolute value of $\text{SNR}_{\Omega, \text{PEM}}(f)$ for 80–160 Hz (left panel) and 460–1000 Hz (right panel) as a function of the week in S5. The horizontal dark (blue) bands correspond to initial frequency notches as described in Step 2 (Sec. V) and vertical dark (blue) lines correspond to unavailability of data due to detector downtime. The large SNR structures seen in the plots were removed from the low- and high-frequency analyses.

time-shift and PEM-coherence methods described in Secs. IV B and IV C to identify any remaining contaminated frequency bins. To remove bad frequency bins, we split the S5 data set into weeklong periods and for each week, we reject any frequency bin for which either $|\text{SNR}_{\Omega, \text{TS}}(f)|$ or $|\text{SNR}_{\Omega, \text{PEM}}(f)|$ exceeds a predetermined threshold in the given week, the corresponding month, or in the entire S5 data set. This procedure generates (different) sets of frequency notchings for each week of the S5 data set. In the analysis we use two different sets of SNR threshold values for the cut, which are further described in Sec. VI.

Figure 4 is a spectrogram of $\text{SNR}_{\Omega, \text{PEM}}$ for the 80–160 Hz band for all weeks in S5; the visible structure represents correlated noise between H1 and H2, which was identified and subsequently excluded from the analysis by the H1-H2 coherence, time-shift, and PEM-coherence measurements.

Note that previous stochastic analyses using LIGO data [26–28,46] followed only Steps 1, 2, and 4. Steps 3 and 5 were developed for this particular analysis.

Having defined the time segments and frequency bins to be rejected in each week of the S5 data, we proceed with the calculation of the estimators and standard errors, $\hat{\Omega}_\alpha(f)$ and $\sigma_{\hat{\Omega}_\alpha}(f)$, in much the same manner as in previous searches for isotropic stochastic backgrounds [26–28,47]. The data is divided into $T = 60$ s segments, decimated to 1024 Hz for the low-frequency analysis and 4096 Hz for the high-frequency analysis, and high-pass filtered with a sixth order Butterworth filter with 32 Hz knee frequency. Each analysis segment is Hann windowed, and to recover the loss of signal-to-noise ratio due to Hann windowing, segments are 50% overlapped. Estimators and standard errors for each segment are evaluated with a $\Delta f = 0.25$ Hz frequency

resolution, using the frequency mask of the week to which the segment belongs. A weighted average is performed over all segments and all frequency bins, with inverse variances, as in Eq. (7), but properly accounting for overlapping.

VI. ANALYSIS RESULTS

The analysis is separated into two parts corresponding to searches for SGWBs with spectral index $\alpha = 0$ and $\alpha = 3$ as described in Sec. III. Since the strain output of an interferometer due to GWs is $S_{\text{gw}}(f) \propto f^{\alpha-3}$ (see Eq. (3)), the case $\alpha = 0$ is dominated by low frequencies while $\alpha = 3$ is independent of frequency. Since for $\alpha = 3$ there is no preferred frequency band, and since previous analyses [46] for stochastic backgrounds with $\alpha = 3$ considered only high frequencies, we also used only high frequencies for the $\alpha = 3$ case. Thus, the two cases of $\alpha = 0$ and $\alpha = 3$ correspond to the analysis of the low- and high-frequency bands, respectively. In this section, we present the results of the analyses in the two different frequency bands as defined in Sec. IV D corresponding to the two different values of α .

To illustrate the effect of the various noise removal methods described in the previous two sections, we give the results as different stages of cuts are applied to the data (see Table I). The threshold value used at stage III comes from an initial study performed using playground data to understand the effectiveness of the PEM-coherence method in finding problematic frequency bins in the H1-H2 analysis, and hence those results are considered as *blind analysis* results. But a post-unblinding study showed that we could lower the SNR_{PEM} threshold to values as low as 0.5 (for low frequency) and 1 (for high frequency), which are used at stage IV. These postblinding results are used in the final

TABLE I. Definition of various stages of noise removal for the high- and low-frequency analyses in terms of the analysis steps described in Sec. V. Here stage III corresponds to the blind analysis and stage IV to the post-unblinding analysis. The percentage of data vetoed accounts for both the time segments and the frequency bins excluded from the analysis. In calculating veto percentage, the analyses with noncolocated LIGO detectors only account for the time segments excluded from the analyses and this is the reason for the large numbers we see in the last column compared to other LIGO analyses.

Stage	High-frequency analysis		Low-frequency analysis	
	Steps	% of data vetoed	Steps	% of data vetoed
I	Step 1	8.51	Step 1	8.51
II	Steps 1–4	35.88	Steps 1–4	56.01
III	Steps 1–5 with $ \text{SNR}_{\text{PEM}} > 2$, $ \text{SNR}_{\text{TS}} > 2$	47.19	Steps 1–5 with $ \text{SNR}_{\text{PEM}} > 2$, $ \text{SNR}_{\text{TS}} > 2$	72.29
IV	Steps 1–5, with $ \text{SNR}_{\text{PEM}} > 1$, $ \text{SNR}_{\text{TS}} > 2$	48.95	Steps 1–5, with $ \text{SNR}_{\text{PEM}} > 0.5$, $ \text{SNR}_{\text{TS}} > 2$	76.60

upper-limit calculations. For threshold values < 0.5 (low frequency) or < 1 (high frequency), the PEM-coherence contribution, $\hat{\Omega}_{\alpha, \text{PEM}}$, varies randomly as the threshold is changed indicating the statistical noise limit of the PEM-coherence method.

A. High-frequency results

We performed the high-frequency analysis with spectral index $\alpha = 3$, and reference frequency $f_{\text{ref}} = 900$ Hz. Tables II and III summarize the results after applying several stages of noise removal as defined in Table I. Table II applies to the full analysis band, 460–1000 Hz;

TABLE II. Results for the H1-H2 high-frequency analysis (460–1000 Hz) after various stages of noise removal were applied to the data. The estimates $\hat{\Omega}_3$, PEM-coherence contribution, $\hat{\Omega}_{3, \text{PEM}}$, and $\sigma_{\hat{\Omega}_3}$ are calculated assuming $H_0 = 68$ km/s/Mpc. $\sigma_{\hat{\Omega}_3}$ is the statistical uncertainty in $\hat{\Omega}_3$. The last column gives the ratio of the standard deviation of the values of the inverse Fourier transform of $\hat{\Omega}_3(f)$ to the statistical uncertainty $\sigma_{\hat{\Omega}_3}$. As described in Sec. VI A, a ratio much $\gg 1$ is a sign of excess cross-correlated noise. ^aThe PEM-coherence estimate on stage I also excludes frequencies (including 60 Hz harmonics) and time segments similar to stages II–IV.

Stage	$\hat{\Omega}_3 (\times 10^{-4})$	$\hat{\Omega}_{3, \text{PEM}} (\times 10^{-4})$	$\sigma_{\hat{\Omega}_3} (\times 10^{-4})$	std/ $\sigma_{\hat{\Omega}_3}$
I	77.5	-3.05^a	2.82	20.5
II	-2.17	-3.62	3.24	1.18
III	-4.11	-4.30	3.59	1.04
IV	-1.29	-2.38	3.64	1.01

TABLE III. Same as Table II, but for five separate subbands of 460–1000 Hz.

Band (Hz)	Stage	$\hat{\Omega}_3 (\times 10^{-4})$	$\hat{\Omega}_{3, \text{PEM}} (\times 10^{-4})$	$\sigma_{\hat{\Omega}_3} (\times 10^{-4})$	std/ $\sigma_{\hat{\Omega}_3}$
460–537	I	-7.28	-0.22	4.48	5.40
	II	-2.17	-0.24	5.08	1.01
	III	-0.60	-1.23	5.68	0.98
	IV	-0.34	-1.23	5.69	0.97
537–628	I	163	-2.28	5.46	24.0
	II	14.7	-2.46	6.32	1.08
	III	8.83	-2.00	6.96	1.02
	IV	8.56	-1.98	7.03	1.02
628–733	I	512	-16.7	7.33	35.9
	II	-33.2	-20.5	8.52	1.37
	III	-37.0	-16.3	9.20	1.21
	IV	-26.5	-5.88	9.66	1.12
733–856	I	-397	-1.77	8.32	23.0
	II	-4.44	-2.24	9.49	1.67
	III	-5.29	-6.40	11.0	1.04
	IV	2.76	-3.91	11.3	0.98
856–1000	I	89.2	4.63	10.6	3.37
	II	2.44	4.63	12.0	1.02
	III	0.004	-1.47	13.2	1.01
	IV	0.21	-1.41	13.2	1.01

Table III gives the results for five separate subbands. The values of the estimator, $\hat{\Omega}_3$, the PEM-coherence contribution to the estimator, $\hat{\Omega}_{3, \text{PEM}}$, and the statistical uncertainty, $\sigma_{\hat{\Omega}_3}$, are given for each band and each stage of noise removal. Also given is the ratio of the standard deviation of the values of the inverse Fourier transform of $\hat{\Omega}_3(f)$ to the statistical uncertainty $\sigma_{\hat{\Omega}_3}$, which is a measure of excess residual correlated noise. In the absence of correlated noise, we expect the distribution of data points in the inverse Fourier transform of $\hat{\Omega}_3(f)$ to follow a Gaussian distribution with mean 0 and std $\sigma_{\hat{\Omega}_3}$. Hence a ratio $\gg 1$ is a sign of excess correlated noise, which shows up as visible structure in the plot of the inverse Fourier transform of $\hat{\Omega}_3(f)$ (for example, see the right-hand plots in Fig. 5). We see that this ratio decreases for the full 460–1000 Hz band and for each subband with every stage of data cleanup indicating the effectiveness of the PEM-coherence SNR cut. We also note that the values listed in Tables II, III, and IV are the zero lag values of $\hat{\Omega}_\alpha$ in the corresponding inverse Fourier transform plots.

Figure 5 is devoted entirely to the noisiest subband, 628–733 Hz. The left column of plots shows $\hat{\Omega}_3(f)$ and $\hat{\Omega}_{3, \text{PEM}}(f)$, with black lines denoting the statistical error bar $\pm \sigma_{\hat{\Omega}_3}(f)$. Here we can clearly see the effectiveness of noise removal through the four stages discussed above. Note the lack of structure near zero lag in the final inverse Fourier transform of the estimator $\hat{\Omega}_3(f)$, which is consistent with no correlated noise. Figure 6 is a similar plot for the full 460–1000 Hz band, showing the results after the final stage of cuts. Again note the lack of significant

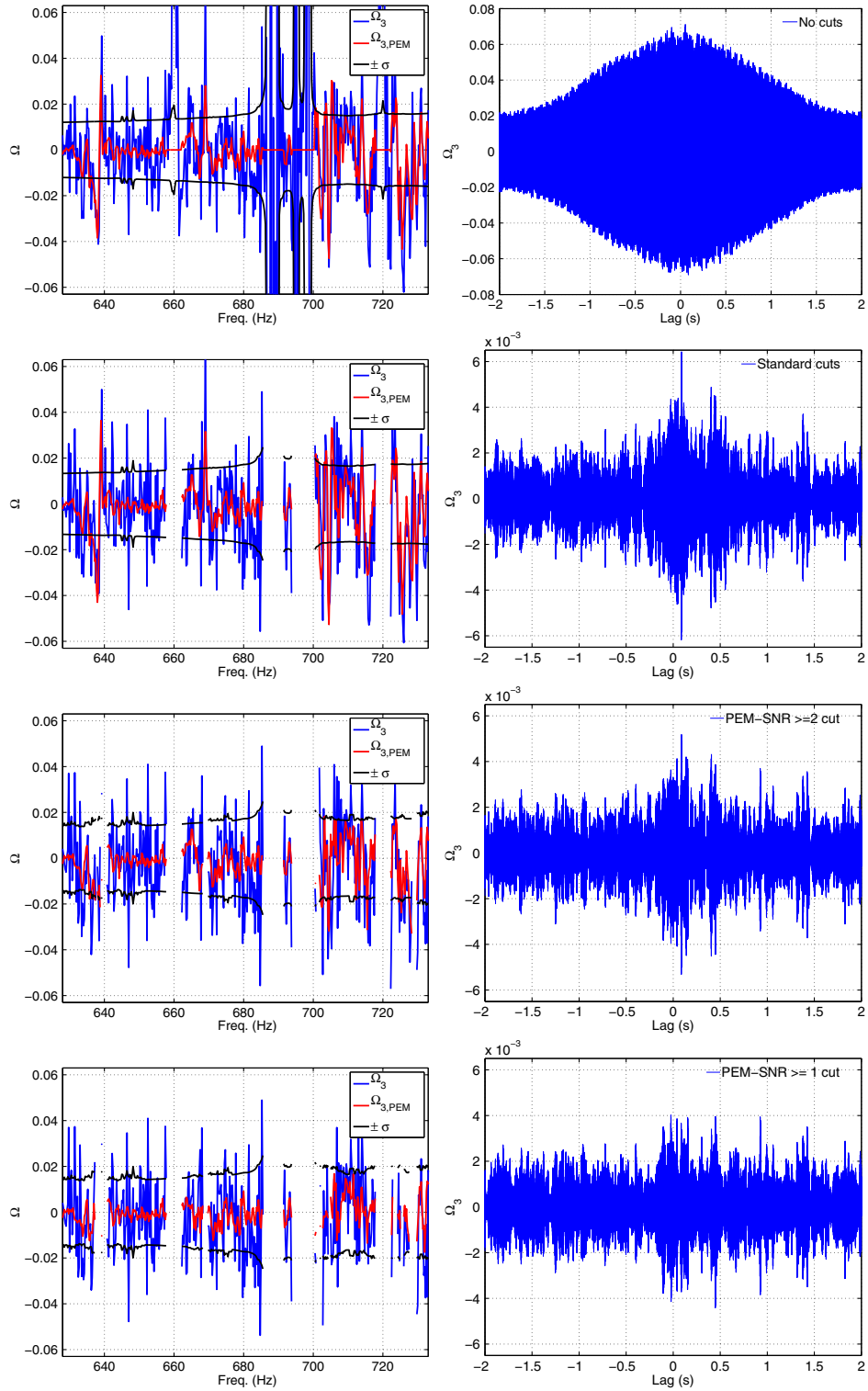


FIG. 5 (color online). Plots of $\hat{\Omega}_3(f)$ and $\hat{\Omega}_{3,PEM}(f)$ (left panels), and the inverse Fourier transform of $\hat{\Omega}_3(f)$ (right panels), for the (noisiest) 628–733 Hz subband after various stages of noise removal were applied to the data. The four rows correspond to the four different stages of cleaning defined in Table I. (The top right plot has y-axis limits $13 \times$ greater than the other three.)

structure near zero lag in the inverse Fourier transform of $\hat{\Omega}_3(f)$. Figure 7 (left panel) shows how the final estimate, $\hat{\Omega}_3$, summed over the whole band, evolves over the course of the run after the final stage of cuts. The smoothness of

that plot (absence of any sharp rise or fall after the accumulation of sufficient data i.e., one month) indicates that no particular time period dominates our final result.

TABLE IV. Similar to Table II but for the low-frequency analysis (80–160 Hz) and for spectral index $\alpha = 0$. The different rows give the results after various stages of noise removal were applied to the data. ^aThe PEM-coherence estimate on stage I also excludes frequencies (including 60 Hz harmonics) and time segments similar to stages II–IV.

Stage	$\hat{\Omega}_0$ ($\times 10^{-6}$)	$\hat{\Omega}_{0, \text{PEM}}$ ($\times 10^{-6}$)	$\sigma_{\hat{\Omega}_0}$ ($\times 10^{-6}$)	std/ $\sigma_{\hat{\Omega}_0}$
I	6.17	-0.39 ^a	0.44	5.90
II	-1.71	-0.78	0.63	1.80
III	-1.57	-0.84	0.79	1.64
IV	-0.26	-0.29	0.85	1.63

B. Low-frequency results

We now repeat the analysis of the previous subsection but for the low-frequency band, 80–160 Hz with spectral index $\alpha = 0$ and $f_{\text{ref}} = 100$ Hz. Table IV summarizes the results for the low-frequency analysis after applying several stages of noise removal as defined in Table I. Figure 8 shows the results obtained by applying the noise removal cuts in four stages. The left column of plots contains the estimators, $\hat{\Omega}_0(f)$ and $\hat{\Omega}_{0, \text{PEM}}(f)$, with lines denoting the statistical error bar $\pm \sigma_{\hat{\Omega}_0}(f)$.

In contrast to the high-frequency analysis (compare Figs. 6 and 8) there is still much structure in the inverse Fourier transform of $\hat{\Omega}_0(f)$ around zero lag even after the final stage of noise removal cuts was applied. In addition, the PEM-coherence contribution to the estimator, $\hat{\Omega}_{0, \text{PEM}}(f)$, displays much of the structure observed in $\hat{\Omega}_0(f)$. Both of these observations suggest contamination from residual correlated instrumental or environmental noise that was not excluded by the noise removal methods. Figure 7 (right panel) shows how the final estimate, $\hat{\Omega}_0$, evolves over the course of the run after the final stage of cuts. We note here that even though $\hat{\Omega}_0$ (last entry in

Table IV) is consistent with zero (within 2σ), its estimate at other nonzero lags vary strongly as shown in Fig. 8 (lower right panel). This indicates the presence of residual correlated noise after all the time-shift and PEM-coherence noise removal cuts are applied.

C. Hardware and software injections

We validated our analysis procedure by injecting simulated stochastic GW signals into the strain data of the two detectors. Both *hardware* and *software* injections were performed. Hardware injections are performed by physically moving the interferometer mirrors coherently between interferometers. In this case the artificial signals were limited to short durations and relatively large amplitudes. The data from these hardware injection times were excluded from the analyses described above, as noted in Sec. V, Step 1. Software injections are conducted by adding a simulated GW signal to the interferometer data, in which case they could be long in duration and relatively weak in amplitude. During S5 there was one stochastic signal hardware injection when both H1 and H2 were operating in coincidence. A stochastic background signal with spectral index $\alpha = 0$ and amplitude $\Omega_0 = 6.56 \times 10^{-3}$ was injected for approximately three hours. In performing the analysis, frequency bins were excluded based on the standard H1-H2 coherence calculations. No additional frequency bins were removed using SNR_{PEM} . The recovered signal was $\Omega_0 = (7.39 \pm 1.1) \times 10^{-3}$, which is consistent with the injected amplitude. Due to the spectral index used for the injection ($\alpha = 0$), the recovery analysis was performed using only the low-frequency band. We also performed a software injection in the high-frequency band with an amplitude $\Omega_3 = 5.6 \times 10^{-3}$, and we recovered it successfully. Figure 9 shows the spectrum of the recovered $\hat{\Omega}_3(f)$ and its inverse Fourier transform.

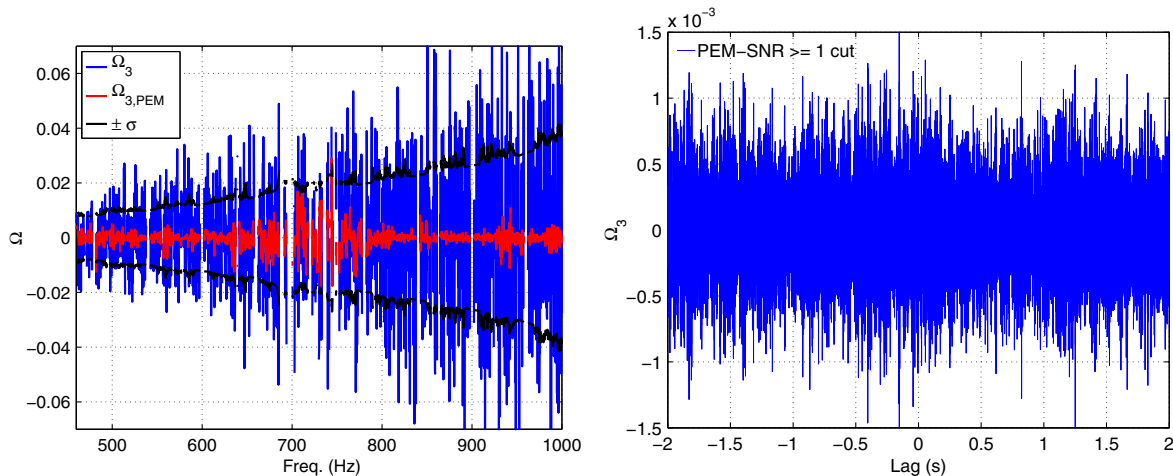


FIG. 6 (color online). Plots of $\hat{\Omega}_3(f)$ and $\hat{\Omega}_{3, \text{PEM}}(f)$ (left panel), and the inverse Fourier transform of complex $\hat{\Omega}_3(f)$ (right panel) for the full band (460–1000 Hz) after the final stage of noise removal cuts.

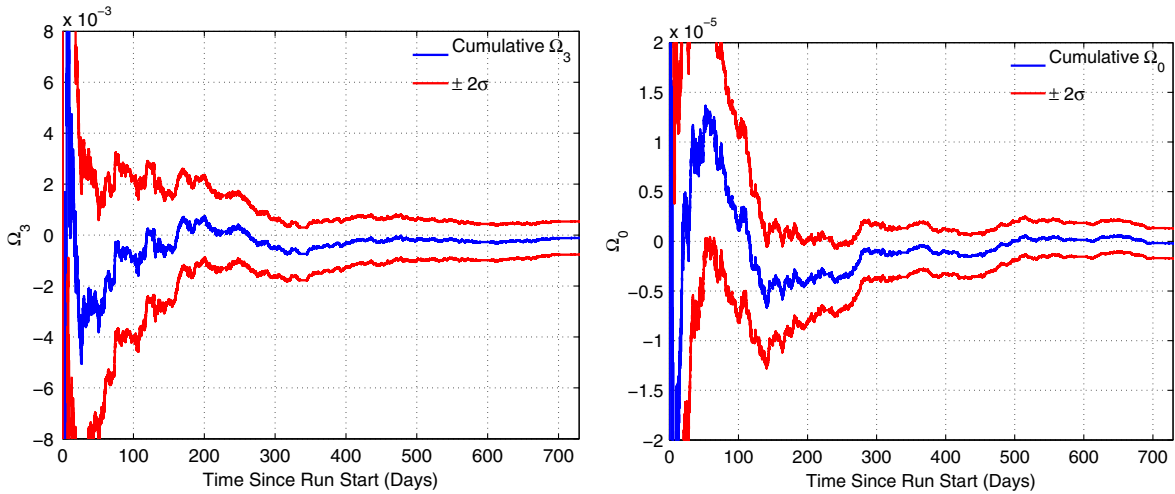


FIG. 7 (color online). Running point estimates $\hat{\Omega}_3$ and $\hat{\Omega}_0$ for the high-frequency (460–1000 Hz) and low-frequency (80–160 Hz) analyses, respectively (left and right panels). The final stage of noise removal cuts has been applied for both analyses.

VII. ASSESSING THE RESIDUAL CORRELATED NOISE

After applying the full noise removal procedure, the high-frequency band appears clean whereas the low-frequency band exhibits evidence of residual correlated noise. In order to interpret the implications of these two very different results, we introduce a general procedure for determining whether a stochastic measurement is sufficiently well understood to yield an astrophysical interpretation. While our immediate concern is to provide a framework for interpreting the two results presented here, we aim to give a comprehensive procedure that can be applied generally, to both colocated and noncolocated detectors. In this spirit, this section is organized as follows: first, we present a general framework for interpreting stochastic measurements; then we discuss how it can be applied to (familiar) results from noncolocated detectors; and finally we apply the framework to our present results.

To determine whether a result can be interpreted as a constraint on the SGWB, we consider the following three criteria:

- (1) We have accounted for all known noise sources through either direct subtraction, vetoing, and/or proper estimation of systematic errors.
- (2) Having accounted for known noise sources, we do not observe evidence of residual noise that is inconsistent with our signal and noise models.
- (3) To the best of our knowledge, there is no plausible mechanism by which broadband correlated noise might be lurking beneath the uncorrelated noise at a level comparable to the GW signal we are trying to measure.

If an analysis result does not meet these criteria, then we conservatively place a bound on the sum of the GW signal and the residual correlated noise. If a result meets all the

criteria, then we present astrophysical bounds on just the GW signal.

Let us now examine these criteria in the context of previous results using the noncolocated LIGO Hanford Observatory (LHO) and LIGO Livingston Observatory (LLO) detectors [28]. Criterion 1 was satisfied by identifying and removing instrumental lines attributable to known instrumental artifacts such as power lines and violin resonances. Criterion 2 was satisfied by creating diagnostic plots, e.g., showing $\hat{\Omega}_0$ vs lag (the delay time between the detectors; see Fig. 5), which demonstrated that the measurement was consistent with uncorrelated noise (and no GW signal). Criterion 3 was satisfied by performing order-of-magnitude calculations for plausible sources of correlated noise for LHO-LLO including electromagnetic phenomena, and finding that they were too small to create broadband correlated noise at a level that is important for initial LIGO.

Next, we consider how the criteria might be applied to future measurements with noncolocated detectors. During the advanced detector era, correlated noise from Schumann resonances may constitute a source of correlated noise at low frequencies $\lesssim 200$ Hz, even for widely separated detector pairs such as LHO-LLO [29,30]. While it may be possible to mitigate this potential correlated noise source through commissioning of the detectors to minimize magnetic coupling, or failing that, through a noise subtraction scheme, we consider the possibility that residual correlated noise is observed. In this scenario, we could still aim to satisfy criteria 2 and 3 by using magnetometer measurements to construct a correlated noise budget, which could then be used to interpret the results.

Finally, we consider how the criteria apply to the measurements presented in this paper. The high-frequency analysis meets criteria 1 and 2 as we did not observe residual noise inconsistent with our noise models

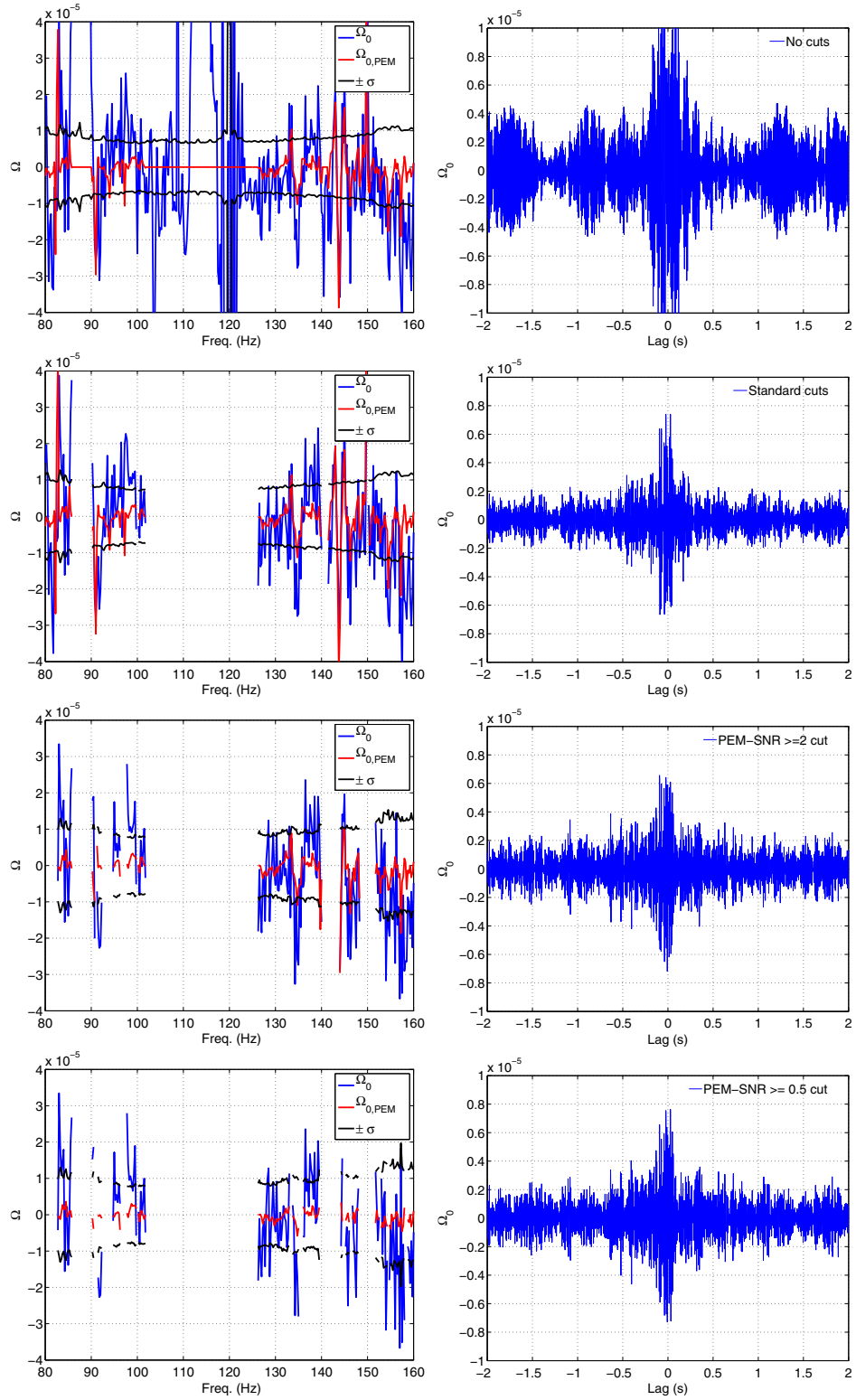


FIG. 8 (color online). Plots of $\hat{\Omega}_0(f)$ and $\hat{\Omega}_{0,PEM}(f)$ (left panels), and the inverse Fourier transform of $\hat{\Omega}_0(f)$ (right panels) for the 80–160 Hz band after various stages of noise removal were applied to the data. The four rows correspond to the four different stages of cleaning defined in Table I.

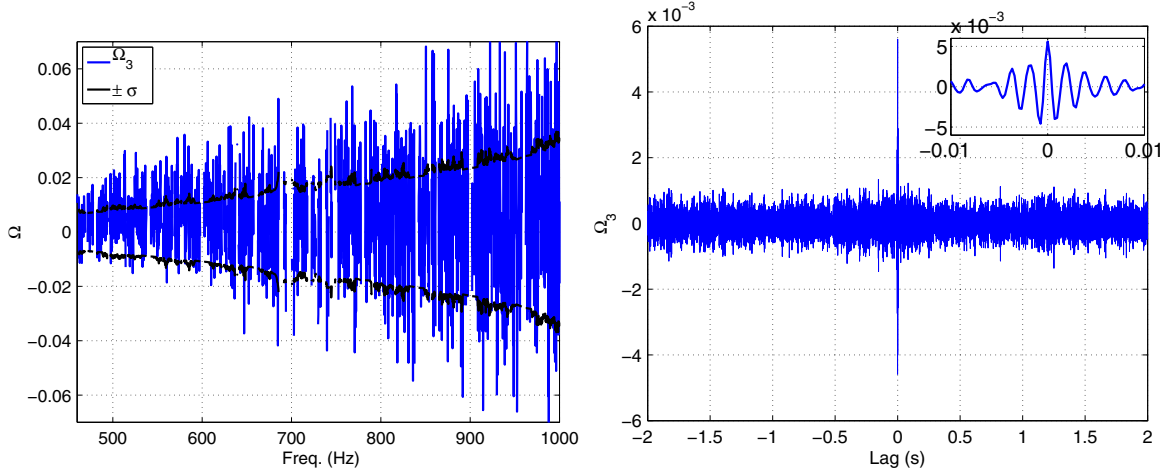


FIG. 9 (color online). (Left panel) Recovered spectrum for a software injection with an amplitude $\Omega_3 = 5.6 \times 10^{-3}$ (SNR ~ 17). (Right panel) The inverse Fourier transform of the recovered $\hat{\Omega}_3(f)$ and a ± 10 ms zoom in around zero lag.

(see Fig. 6). We did observe residual noise for the low-frequency analysis (see Fig. 8), but it was consistent with a preliminary noise model, based on measured acoustic coupling and microphone signals (most of the channels identified by the PEM coherence method were either microphones or accelerometers placed on optical tables that were susceptible to acoustic couplings). While the bands that were acoustically loudest (containing certain electronics fans) were vetoed, the acoustic coupling in between the vetoed bands was high enough to produce a residual signal. We did not further develop the noise model to meet criterion 1 because, with the systematic error from acoustic coupling, the astrophysical limit would not have improved on values we have reported previously [28,48]. For this reason, we do not present an astrophysical limit for the low-frequency band.

We addressed criterion 3 in two ways. First, by investigating mechanisms that might produce unmonitored broadband correlations between detectors, such as the study of correlations introduced by the shared data acquisition system, the study of correlations introduced by light scattering, and PEM coverage studies described in Sec. IV E.

We also identified the sources of most of the features between 80 and 400 Hz. For many of the spectral peaks, in addition to coherence between the GW channels, there was also coherence between the individual GW channels and the accelerometer and microphone signals from the vertex area shared by both detectors. The coupling was consistent with the measured coupling of acoustic signals to the detectors. Most of these features were traced to electronics cooling fans in specific power supply racks in the vertex station by comparing coherence spectra to spectra for accelerometers mounted temporarily on each of the electronics racks. The features were produced at harmonics of the fan rotation frequencies.

The second type of coherence feature was associated with bilinear coupling of low-frequency (< 15 Hz) seismic motion and harmonics of 60 Hz, producing sideband features around the harmonics that were similar to the features in the 0–15 Hz seismic band. Coherence of sideband features was expected since the coherence length of low-frequency seismic signals was greater than the distance separating sensitive parts of the two interferometers at the vertex station, and the seismic isolation of the interferometers was minimal below 10 Hz.

In conclusion, we found no peaks or features in the coherence spectrum for the two GW channels that were inconsistent with linear acoustic coupling or bilinear coupling of low-frequency seismic noise and 60 Hz harmonics at the vertex station. Neither of these mechanisms is capable of producing broadband coherence that is not well monitored by the PEM system. Therefore, for the high-frequency analysis, we satisfy the three criteria for presenting astrophysical bounds on just the GW signal.

A. Upper limits

Since there is no evidence of significant residual noise contaminating the high-frequency data after applying the full set of cuts, we set a 95% confidence level Bayesian upper limit on Ω_3 . We use the previous high-frequency upper limit $\Omega_3 < 0.35$ (adjusted for $H_0 = 68$ km/s/Mpc) from the LIGO S5 and Virgo VSR1 analysis [46] as a prior and assume a flat distribution for Ω_3 from 0 to 0.35. We also marginalize over the calibration uncertainty for the individual detectors (10.2% and 10.3% for H1 and H2, respectively). In order to include in our calculation the PEM estimate of residual contamination, we take $\sigma_{\hat{\Omega}_3}^2 + \hat{\Omega}_{3,\text{PEM}}^2$ as our total variance. We note here that the estimated $\hat{\Omega}_{3,\text{PEM}}$ is within the observed $\sigma_{\hat{\Omega}_3}$ i.e., we observe no evidence of excess environmental

TABLE V. 95% confidence level upper limits for the full band (460–1000 Hz) and for five separate subbands.

Band (Hz)	95% C.L. UL ($\times 10^{-3}$)
460–1000	0.77
460–537	1.11
537–628	2.12
628–733	1.18
733–856	2.53
856–1000	2.61

contamination and the above quadrature addition increases the limit by $\sim 20\%$. The final result is $\Omega_3 < 7.7 \times 10^{-4}$ for the frequency band 460–1000 Hz, which is an improvement by a factor of ~ 180 over the recent S6/VSR2-3 result [48]. All of the above ~ 180 factor improvement comes from the nearly unity overlap reduction function of the colocated Hanford detectors. In fact, all other data being the same, if we were to consider that the H2 detector not being located at Hanford but instead at the LIGO Livingston site yields an upper limit that is worse by a factor of ~ 1.7 than the S6/VSR2-3 result. Most of this difference of ~ 1.7 comes from the improved sensitivities of S6/VSR2-3 detectors compared to S5 H1-H2 detectors. Upper limits for the five separate subbands of the high-frequency analysis are given in Table V.

As mentioned in Sec. VI B, the structure in the inverse Fourier transform plots of Fig. 8 suggests contamination from residual correlated noise for the low-frequency analysis and hence we do not set any upper limit on Ω_0 using the low-frequency band 80–160 Hz.

VIII. SUMMARY AND PLANS FOR FUTURE ANALYSES

In this paper, we described an analysis for a SGWB using data taken by the two colocated LIGO Hanford detectors, H1 and H2, during LIGO’s fifth science run. Since these detectors share the same local environment, it was necessary to account for the presence of correlated instrumental and environmental noise. We applied several noise identification and mitigation techniques to reduce contamination and to estimate the bias due to any residual correlated noise. The methods proved to be useful in cleaning the high-frequency band, but not enough in the low-frequency band.

In the 80–160 Hz band, we were unable to sufficiently mitigate the effects of correlated noise, and hence we did not set any limits on the GW energy density for $\alpha = 0$. For the 460–1000 Hz band, we were able to mitigate the effects of correlated noise, and so we placed a 95% C.L. upper limit on the GW energy density alone in this band of $\Omega_3 < 7.7 \times 10^{-4}$. This limit improves on the previous best limit in the high-frequency band by a factor of ~ 180 [48]. Figure 10 shows upper limits from current/past SGWB analyses, as well as limits from various SGWB models, and

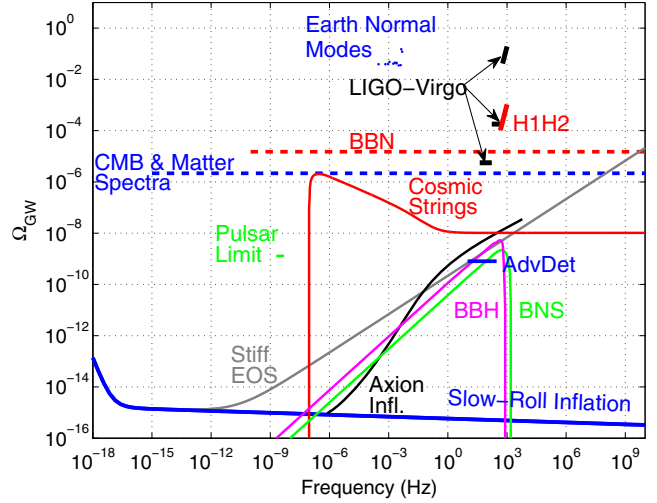


FIG. 10 (color online). Upper limits from the current H1-H2 analysis, previous SGWB analyses and the projected advanced LIGO limit, along with various SGWB models. The BBN limit is an integral limit on Ω_{gw} i.e., $\int \Omega_{\text{gw}}(f)d(\ln f)$ in the 10^{-10} – 10^{10} Hz band derived from the big bang nucleosynthesis and observations of the abundance of light nuclei [28,49]. The measurements of CMB and matter power spectra provide a similar integral bound in the frequency range of 10^{-15} – 10^{10} Hz [50]. The pulsar limit is a bound on the $\Omega_{\text{gw}}(f)$ at $f = 2.8$ nHz and is based on the fluctuations in the pulse arrival times from millisecond pulsars [51]. In the above figure, the slow-roll inflationary model [52] assumes a tensor-to-scalar ratio of $r = 0.2$, the best fit value from the BICEP2 analysis [13]. In the axion based inflationary model, for certain ranges of parameters the backreaction during the final stages of inflation is expected to produce strong GWs at high frequencies [53]. The stiff equation of state (EOS) limit corresponds to scenarios in the early Universe (prior to BBN) in which GWs are produced by an unknown “stiff” energy [54]. For the above figure we used the equation of state parameter $w = 0.6$ in the stiff EOS model. The cosmic string model corresponds to GWs produced by cosmic strings in the early Universe [55]. The Earth’s normal mode limits are based on the observed fluctuations in the amplitudes of Earth’s normal modes using an array of seismometers [56]. The astrophysical SGWBs (BBH and BNS) are due to the superposition of coalescence GW signals from a large number of binary black holes (BBH) and binary neutron stars (BNS) [57].

projected limits using advanced LIGO. We note here that the indirect limits from big bang nucleosynthesis (BBN) apply to SGWBs present in the early Universe at the time of BBN [and characterized by an $\alpha = 0$ power law; see Eq. (2)], but not to SGWBs of astrophysical origin created more recently (and assumed to be characterized by an $\alpha = 3$ power law). Thus, the results presented here complement the indirect bound from BBN, which is only sensitive to cosmological SGWBs from the early Universe, as well as direct $\alpha = 0$ measurements using lower-frequency observation bands [28].

There are several ways in which the methods presented in this paper can be improved. We list some ideas below:

- (i) As mentioned in Sec. IV C, we can improve the estimate of the PEM contribution to the coherence by allowing for correlations between different PEM channels \tilde{z}_I and \tilde{z}_J . This requires inverting the full matrix of PEM coherences $\gamma_{IJ}(f)$ or solving a large number of simultaneous equations involving $\gamma_{IJ}(f)$, rather than simply taking the maximum of the product of the coherences as was done here. A computationally cheaper alternative might be to invert a submatrix formed from the largest PEM contributors—i.e., those PEM channels that contribute the most to the coherence.
- (ii) We can use *bicoherence* techniques to account for (nonlinear) up-conversion processes missed by standard coherence calculations. This may allow us to identify cases where low-frequency disturbances excite higher-frequency modes in the detector.
- (iii) The estimators $\hat{\Omega}_\alpha(f)$ used in this analysis are optimal in the *absence* of correlated noise. In the presence of correlated noise, these estimators are biased, with expected values given by the sum, $\Omega_\alpha + \eta_\alpha(f)$, where the second term involves the cross spectrum, $N_{12}(f)$, of the noise contribution to the detector output. An alternative approach is to start with a likelihood function for the detector output \tilde{s}_1, \tilde{s}_2 , where we allow (at the outset) for the presence of cross-correlated noise. (This would show up in the covariance matrix for a multivariate Gaussian distribution.) We can parametrize $N_{12}(f)$ in terms of its amplitude, spectral index, etc., and then construct posterior distributions for these parameters along with the amplitude and spectral index of the stochastic GW signal. In this (Bayesian) approach, the cross-correlated noise is treated on the same footing as the stochastic GW and is estimated (via its posterior distribution) as part of the analysis [58]. However, as described in [59], this works only for those cases where the spectral shapes of the noise and signal are different from one another.
- (iv) We can also reduce correlated noise by first removing as much noise as possible from the output of the individual detectors. Wiener filtering techniques can be applied to remove acoustic, magnetic, and gravity-gradient noise from the time-series output of the LIGO detectors [60–62]. Furthermore, feed-forward

control can be used to to cancel seismically induced motion before it affects the LIGO test masses [61].

These and/or other techniques might be needed for future cross-correlation searches using advanced detectors, where improved (single-detector) sensitivity will mean that correlated noise may be an issue even for physically separated detectors, such as the LIGO Hanford–LIGO Livingston detector pair [29,30,63].

ACKNOWLEDGMENTS

The authors gratefully acknowledge the support of the U.S. National Science Foundation for the construction and operation of the LIGO Laboratory, the Science and Technology Facilities Council of the United Kingdom, the Max-Planck-Society, and the State of Niedersachsen/Germany for support of the construction and operation of the GEO600 detector, and the Italian Istituto Nazionale di Fisica Nucleare and the French Centre National de la Recherche Scientifique for the construction and operation of the Virgo detector. The authors also gratefully acknowledge the support of the research by these agencies and by the Australian Research Council, the International Science Linkages program of the Commonwealth of Australia, the Council of Scientific and Industrial Research of India, the Istituto Nazionale di Fisica Nucleare of Italy, the Spanish Ministerio de Economía y Competitividad, the Conselleria d'Economia Hisenda i Innovació of the Govern de les Illes Balears, the Foundation for Fundamental Research on Matter supported by the Netherlands Organisation for Scientific Research, the Polish Ministry of Science and Higher Education, the FOCUS Programme of Foundation for Polish Science, the Royal Society, the Scottish Funding Council, the Scottish Universities Physics Alliance, The National Aeronautics and Space Administration, OTKA of Hungary, the Lyon Institute of Origins (LIO), the National Research Foundation of Korea, Industry Canada and the Province of Ontario through the Ministry of Economic Development and Innovation, the National Science and Engineering Research Council Canada, the Carnegie Trust, the Leverhulme Trust, the David and Lucile Packard Foundation, the Research Corporation, and the Alfred P. Sloan Foundation.

[1] L. P. Grishchuk, JETP Lett. **23**, 293 (1976).
 [2] A. A. Starobinskii, JETP Lett. **30**, 682 (1979).
 [3] R. Bar-Kana, Phys. Rev. D **50**, 1157 (1994).
 [4] M. Maggiore, Phys. Rep. **331**, 283 (2000).
 [5] B. Abbott *et al.*, Rep. Prog. Phys. **72**, 076901 (2009).

[6] F. Acernese *et al.*, Classical Quantum Gravity **25**, 114045 (2008).
 [7] B. Willke *et al.*, Classical Quantum Gravity **23**, S207 (2006).
 [8] P. Bender, K. Danzmann, and the LISA Study Team, LISA Project Report No. MPQ233, 1998.

- [9] E. Phinney *et al.*, *The Big Bang Observer: Direct Detection of Gravitational Waves from the Birth of the Universe to the Present* (NASA, Washington, D.C., 2004).
- [10] F. A. Jenet, G. B. Hobbs, W. van Straten, R. N. Manchester, M. Bailes, J. P. W. Verbiest, R. T. Edwards, A. W. Hotan, J. M. Sarkissian, and S. M. Ord, *Astrophys. J.* **653**, 1571 (2006).
- [11] R. van Haasteren *et al.*, *Mon. Not. R. Astron. Soc.* **414**, 3117 (2011).
- [12] B. Allen, in *Proceedings of the Les Houches School on Astrophysical Sources of Gravitational Waves* (Cambridge University Press, Cambridge, England, 1997), p. 373.
- [13] P. A. R. Ade *et al.* (BICEP2 Collaboration), *Phys. Rev. Lett.* **112**, 241101 (2014).
- [14] R. Flauger, J. C. Hill, and D. N. Spergel, *J. Cosmol. Astropart. Phys.* **08** (2014) 039.
- [15] M. J. Mortonson and U. Seljak, *J. Cosmol. Astropart. Phys.* **10** (2014) 035.
- [16] T. Regimbau and J. de Freitas Pacheco, *Astron. Astrophys.* **447**, 1 (2006).
- [17] T. Regimbau and J. de Freitas Pacheco, *Astron. Astrophys.* **376**, 381 (2001).
- [18] T. Regimbau and J. A. de Freitas Pacheco, *Astrophys. J.* **642**, 455 (2006).
- [19] T. Regimbau and B. Chauvineau, *Classical Quantum Gravity* **24**, S627 (2007).
- [20] X.-J. Zhu, E. Howell, T. Regimbau, D. Blair, and Z.-H. Zhu, *Astrophys. J.* **739**, 86 (2011).
- [21] A. Jaffe and D. Backer, *Astrophys. J.* **583**, 616 (2003).
- [22] P. Michelson, *Mon. Not. R. Astron. Soc.* **227**, 933 (1987).
- [23] N. Christensen, *Phys. Rev. D* **46**, 5250 (1992).
- [24] E. E. Flanagan, *Phys. Rev. D* **48**, 2389 (1993).
- [25] B. Allen and J. D. Romano, *Phys. Rev. D* **59**, 102001 (1999).
- [26] B. Abbott *et al.*, *Phys. Rev. D* **69**, 122004 (2004).
- [27] B. Abbott *et al.*, *Astrophys. J.* **659**, 918 (2007).
- [28] B. Abbott *et al.*, *Nature (London)* **460**, 990 (2009).
- [29] E. Thrane, N. Christensen, and R. M. S. Schofield, *Phys. Rev. D* **87**, 123009 (2013).
- [30] E. Thrane, N. Christensen, R. M. S. Schofield, and A. Effler, *Phys. Rev. D* **90**, 023013 (2014).
- [31] B. Abbott *et al.*, *Nucl. Instrum. Methods Phys. Res., Sect. A* **517**, 154 (2004).
- [32] L. Blackburn *et al.*, *Classical Quantum Gravity* **25**, 184004 (2008).
- [33] N. Christensen, P. Shawhan, and G. González for (the LIGO Scientific Collaboration), *Classical Quantum Gravity* **21**, S1747 (2004).
- [34] A. diCredico (for the LIGO Scientific Collaboration), *Classical Quantum Gravity* **22**, S1051 (2005).
- [35] N. Christensen (for the LIGO Scientific Collaboration), *Classical Quantum Gravity* **22**, S1059 (2005).
- [36] B. Abbott *et al.*, *Classical Quantum Gravity* **24**, 5343 (2007).
- [37] B. Abbott *et al.*, *Phys. Rev. Lett.* **102**, 111102 (2009).
- [38] B. Abbott *et al.*, *Phys. Rev. D* **80**, 042003 (2009).
- [39] L. Grishchuk, *Sov. Phys. Usp.* **31**, 940 (1988).
- [40] P. A. R. Ade *et al.*, *Astron. Astrophys.* **571**, A1 (2014).
- [41] For other pairs such as H1-L1, $\gamma(f)$ could be zero at some frequencies. Since both $\hat{\Omega}_\alpha(f)$ and $\sigma_{\hat{\Omega}_\alpha}(f)$ have $\gamma(f)$ in their denominators, the final result obtained by the weighted average [Eq. (7)] is always finite.
- [42] For ease of notation, we do not explicitly show the time dependence of the estimators.
- [43] N. V. Fotopoulos (for the LIGO Scientific Collaboration), *J. Phys. Conf. Ser.* **122**, 012032 (2008).
- [44] N. V. Fotopoulos (for the LIGO Scientific Collaboration), *Classical Quantum Gravity* **23**, S693 (2006).
- [45] S. Chatterji, L. Blackburn, G. Martin, and E. Katsavounidis, *Classical Quantum Gravity* **21**, S1809 (2004).
- [46] J. Abadie *et al.*, *Phys. Rev. D* **85**, 122001 (2012).
- [47] B. Abbott *et al.*, *Phys. Rev. Lett.* **95**, 221101 (2005).
- [48] J. Aasi *et al.* (LIGO Scientific and VIRGO Collaborations), *Phys. Rev. Lett.* **113**, 231101 (2014).
- [49] R. H. Cyburt, B. D. Fields, K. A. Olive, and E. Skillman, *Astropart. Phys.* **23**, 313 (2005).
- [50] I. Sendra and T. L. Smith, *Phys. Rev. D* **85**, 123002 (2012).
- [51] R. M. Shannon, V. Ravi, W. A. Coles, G. Hobbs, M. J. Keith, R. N. Manchester, J. S. B. Wyithe, M. Bailes, N. D. R. Bhat, S. Burke-Spolaor *et al.*, *Science* **342**, 334 (2013).
- [52] M. S. Turner, *Phys. Rev. D* **55**, R435 (1997).
- [53] N. Barnaby, E. Pajer, and M. Peloso, *Phys. Rev. D* **85**, 023525 (2012).
- [54] L. A. Boyle and A. Buonanno, *Phys. Rev. D* **78**, 043531 (2008).
- [55] X. Siemens, V. Mandic, and J. Creighton, *Phys. Rev. Lett.* **98**, 111101 (2007).
- [56] M. Coughlin and J. Harms, *Phys. Rev. D* **90**, 042005 (2014).
- [57] C. Wu, V. Mandic, and T. Regimbau, *Phys. Rev. D* **85**, 104024 (2012).
- [58] E. Robinson and A. Vecchio, Report No. LIGO-P1100107, 2011.
- [59] M. R. Adams and N. J. Cornish, *Phys. Rev. D* **89**, 022001 (2014).
- [60] B. Allen, W. Hua, and A. Ottewill, [arXiv:gr-qc/9909083](https://arxiv.org/abs/gr-qc/9909083).
- [61] J. C. Driggers, M. Evans, K. Pepper, and R. Adhikari, *Rev. Sci. Instrum.* **83**, 024501 (2012).
- [62] J. C. Driggers, J. Harms, and R. X. Adhikari, *Phys. Rev. D* **86**, 102001 (2012).
- [63] N. L. Christensen, Ph.D. thesis, Massachusetts Institute of Technology, 1990.